

## Supplementary Information

### High Stability of Ultra-small and Isolated Gold Nanoparticles in Metal-Organic Framework Materials

Jérémy Cure<sup>1,2</sup>, Eric Mattson<sup>1</sup>, Kévin Cocq<sup>3</sup>, Hala Assi<sup>3</sup>, Stephanie Jensen<sup>4</sup>, Kui Tan<sup>1</sup>, Massimo Catalano<sup>1,5</sup>, Shuai Yuan<sup>6</sup>, Hao Wang<sup>7</sup>, Liang Feng<sup>6</sup>, Peng Zhang<sup>6</sup>, Sunah Kwon<sup>1</sup>, Jean-François Veyan<sup>1</sup>, Yasiel Cabrera<sup>1</sup>, Guoyu Zhang<sup>7</sup>, Jing Li<sup>7</sup>, Moon Kim<sup>1</sup>, Hong-Cai Zhou<sup>6,8</sup>, Yves J. Chabal<sup>1,\*</sup>, and Timo Thonhauser<sup>4,\*</sup>

<sup>1</sup>Department of Materials Science and Engineering, University of Texas at Dallas, Richardson, TX (USA)

<sup>2</sup>LAAS-CNRS, University of Toulouse, 7 avenue du Colonel Roche, 31031 Toulouse, France

<sup>3</sup>LCC-CNRS, University of Toulouse, 205 route de Narbonne, 31077 Toulouse, France

<sup>4</sup>Department of Physics and Center for Functional Materials, Wake Forest University, Winston-Salem, NC (USA)

<sup>5</sup>Istituto Microelettronica e Microsistemi del Consiglio Nazionale delle Ricerche, Via Monteroni, 73100 Lecce, Italy

<sup>6</sup>Department of Chemistry, Texas A&M University, College Station, TX (USA)

<sup>7</sup>Department of Chemistry and Chemical Biology, Rutgers University, Piscataway, NJ (USA)

<sup>8</sup>Department of Materials Sciences and Engineering, Texas A&M University, College Station, TX (USA)

# Table of Contents

<b>SECTION A – MATERIALS AND SYNTHESIS</b> .....	3
<b>A-1. Materials and Reagents</b> .....	3
<b>A-2. Synthesis of MOFs and Au/MOFs materials</b> .....	3
<i>A-2.1. Synthesis of <math>[Zr_6O_4(OH)_4](H_2O(OH))_6(btc)_6</math> (MOF-808)</i> .....	3
<i>A-2.2. Synthesis of <math>[Zr_6O_4(OH)_4](btc)_6(paba)_6</math> (MOF-808-NH<sub>2</sub>) and <math>Zr_6O_4(OH)_4(btc)_6(pmba)_6</math> (MOF-808-SH)</i> .....	4
<i>A-2.3. Synthesis of <math>[Cr_3OF(H_2O)_2](bdc)_3</math> (MIL-101 (Cr))</i> .....	4
<i>A-2.4. Synthesis of MIL-101 (Cr) -SH</i> .....	5
<i>A-2.5. Synthesis of <math>[Zr_6O_4(OH)_4](bdc)_6</math> (UiO-66)</i> .....	6
<i>A-2.6. Synthesis of Au/MOFs materials</i> .....	6
<i>A-2.7. Titanium doping on MOF-808-SH</i> .....	7
<b>SECTION B – CHARACTERIZATION TECHNIQUES</b> .....	8
<b>SECTION C – EXPERIMENTAL MEASUREMENTS AND THEORETICAL MODELING</b> ..	10
<b>C-1. Brunauer-Emmett-Teller (BET) results of Au/MOFs and MOFs materials</b> .....	10
<b>C-2. HRTEM observations of Au/MOFs materials</b> .....	16
<i>C-2.1. Au NPs mean diameters measurements</i> .....	16
<i>C-2.2. Correlation between the Au NP diameters and the pores widths in the MOF-808 series</i> .....	18
<i>C-2.3. Correlation between the Au NP diameters and the pores widths of the host MOFs</i> .....	19
<i>C-2.4. Effects of ultrasounds on the Au NPs mean size</i> .....	19
<i>C-2.5. Stabilization of Au NPs in Au/MOF-808-SH after 9 months</i> .....	21
<b>C-3. XPS spectra of Au/MOFs and MOFs materials</b> .....	22
<b>C-4. XRD diagrams of Au/MOF and MOFs materials</b> .....	37
<b>C-5. UV-vis spectra of Au/MOF materials</b> .....	41
<b>C-6. LEIS spectra of Au/MOFs and MOFs materials</b> .....	43
<b>C-7. Ab initio calculations performed on Au/MOF-808-SH</b> .....	46
<b>C-8. IR and Raman spectroscopic study of Au/MOFs and MOFs materials</b> .....	50
<i>C-8.1. Evidence of Au-O stretch mode</i> .....	50
<i>C-8.2. Evidence of interaction between the carboxylate groups and Au NPs</i> .....	55
<b>C-9. Influence of the functionalization by -SH groups on the strong stabilization of Au NPs in MIL-101 (Cr) -SH</b> .....	61
<b>C-10. Characterization of Ti transmetalated Zr-based MOFs materials</b> .....	62
<b>C-11. Rate measurement of hydrogen production</b> .....	69
<b>C-12. Additional Characterization of Au/MOF-808-SH after photocatalysis</b> .....	71
<b>C-13. XPS depth profile of Au/MOF-808-SH (Ti) before and after photocatalysis</b> .....	73
<b>REFERENCES</b> .....	76

## SECTION A – MATERIALS AND SYNTHESIS

### A-1. Materials and Reagents

$\text{Cu}_3(\text{bdc})_2(\text{H}_2\text{O})_3$  (Basolite® C 300, HKUST-1), the metal precursors:  $\text{HAuCl}_4 \cdot 3\text{H}_2\text{O}$ ,  $\text{TiCl}_4$ ,  $\text{ZrOCl}_2 \cdot 8\text{H}_2\text{O}$ ,  $\text{ZrCl}_4$ ,  $\text{Cr}(\text{NO}_3)_3 \cdot 9\text{H}_2\text{O}$  and benzene-1,4-dicarboxylic acid ( $\text{H}_2\text{bdc}$ ), benzene-1,3,5-tricarboxylic acid ( $\text{H}_3\text{btc}$ ), *para*-aminobenzoic acid (paba) and *para*-mercaptobenzoic acid (pmba), dimethylformamide (DMF), ethanol reagent grade, acetone, formic acid, nitric acid and hydrochloric acid are supplied by Sigma-Aldrich.

### A-2. Synthesis of MOFs and Au/MOFs materials

#### A-2.1. Synthesis of $[\text{Zr}_6\text{O}_4(\text{OH})_4](\text{H}_2\text{O}(\text{OH}))_6(\text{btc})_6$ (MOF-808)

Microcrystalline powder samples of MOF-808 were prepared using slightly modified published procedures.<sup>1</sup>  $\text{H}_3\text{btc}$  (210 mg, 1 mmol) and  $\text{ZrOCl}_2 \cdot 8\text{H}_2\text{O}$  (970 mg, 3 mmol) were dissolved in DMF/formic acid (45 mL/45 mL) and placed in a 100 mL screw-capped glass jar, which was heated to 130 °C for two days. A white precipitate was collected by filtration and washed three times with 20 mL of fresh DMF. As-synthesized MOF-808 was then immersed in 10 mL of anhydrous DMF for three days, during which time the DMF was replaced three times per day. The DMF-exchanged compound was filtrated off and immersed in 10 mL of water for three days, during which time the water was replaced three times per day. Water exchanged material was then immersed in 10 mL of anhydrous acetone for three days, during which time the acetone was replaced three times per day. The acetone-exchanged sample was then evacuated at room temperature for 24 h and at 150 °C for 24 h to yield activated sample.

*A-2.2. Synthesis of  $[Zr_6O_4(OH)_4](btc)_6(paba)_6$  (MOF-808-NH<sub>2</sub>) and  $Zr_6O_4(OH)_4(btc)_6(pmba)_6$  (MOF-808-SH)*

The activated MOF-808 sample (100 mg) was treated with an excess 4-aminobenzoic acid/DMF solution at 65 °C for 24 h to yield MOF-808-NH<sub>2</sub> sample. The MOF-808-NH<sub>2</sub> was first immersed in 10 mL of anhydrous DMF for two days and then washed with anhydrous acetone several times. The acetone-exchanged sample was evacuated at room temperature for 24 h and at 150 °C for 24 h to yield activated sample. MOF-808-SH was prepared in a similar way, using 4-mercaptopbenzoic acid instead.

*A-2.3. Synthesis of  $[Cr_3OF(H_2O)_2](bdc)_3$  (MIL-101 (Cr))*

MIL-101 (Cr) was synthesized according to the reported procedure with slight modifications.<sup>2</sup> Typically, a solution containing chromium(III) nitrate Cr(NO<sub>3</sub>)<sub>3</sub>·9H<sub>2</sub>O (800 mg, 2.0 mmol), HNO<sub>3</sub> (2.0 mmol), benzene-1,4-dicarboxylic acid (328 mg, 2.0 mmol), and 10 mL H<sub>2</sub>O was transferred to the PTFE/Teflon liner in a hydrothermal autoclave which is heated at 210 °C for 8 h and cooled afterwards slowly to room temperature. The solid product was isolated as a green powder by centrifugation and washed three times with DMF, water, ethanol for 12 h at 80 °C, respectively. The final product was dried under vacuum at 150 °C for 24 h.

#### *A-2.4. Synthesis of MIL-101 (Cr) -SH*

According to the reported procedure,<sup>3</sup> the synthesis of MIL-101 (Cr) -SH requires 5 synthesis steps as described below.

##### *a) Synthesis of MIL-101 (Cr) -NO<sub>2</sub>*

From MIL-101 (Cr), the nitration reaction is realized by using a mixture solution of concentrated HNO<sub>3</sub> and concentrated H<sub>2</sub>SO<sub>4</sub> (5:7 v/v) to obtain MIL-101 (Cr) -NO<sub>2</sub>.

##### *b) Synthesis of MIL-101 (Cr) -NH<sub>2</sub>*

From MIL-101 (Cr) -NO<sub>2</sub>, the nitro groups are reduced to amino groups by using tin chloride, as reported in the literature.<sup>4</sup>

##### *c) Synthesis of MIL-101 (Cr) -N<sub>2</sub><sup>+</sup> BF<sub>4</sub><sup>-</sup>*

100 mg of MIL-101 (Cr) -NH<sub>2</sub> is suspended in 20% HBF<sub>4</sub> aqueous solution (2 mL) and diazotized by addition of a solution of NaNO<sub>2</sub> (45 mg) in water 1.6 mL) at 0 °C. The reaction is stirred for another 3 h. Then the solid sample obtained is separated by centrifugation and washed with methanol.<sup>3</sup>

##### *d) Synthesis of MIL-101 (Cr) -OH*

4-hydroxymethyl-styrene (1 mmol), CaCO<sub>3</sub> (0.05 mmol) and Pd(OAc)<sub>2</sub> (0.005 mmol) are added to a suspension of MIL-101 (Cr) -N<sub>2</sub><sup>+</sup> BF<sub>4</sub><sup>-</sup> previously obtained (50 mg, 0.1 mmol) in methanol (1 mL), and the reaction mixture is stirred at room temperature for 24 hours. The solid sample obtained is separated by centrifugation and washed successively with 5% HNO<sub>3</sub>, methanol and dichloromethane. Finally, the green solid is dried under vacuum at 60 °C for 8 h to give the desired MIL-101 (Cr) -OH.<sup>3</sup>

##### *e) Synthesis of MIL-101 (Cr) -SH*

SOCl<sub>2</sub> (118 mg, 1 mmol) is added dropwise to a suspension of MIL-101 (Cr) -OH (200 mg) in dichloromethane (5 mL) at 0 °C. The reaction mixture is stirred for 1 h. Then the solid sample obtained is separated by centrifugation and washed successively with

dichloromethane and tetrahydrofuran. The greenish solid thus obtained is dried under vacuum at 60 °C for 12 h and then suspended in anhydrous tetrahydrofuran (2 mL). To this suspension, potassium thioacetate (114 mg, 1 mmol) and potassium carbonate (148 mg, 1 mmol) are added and stirred at room temperature overnight. The solid is collected by centrifugation and washed with anhydrous tetrahydrofuran. The solid is then suspended in methanol (5 mL) before adding potassium carbonate (74 mg, 0.5 mmol), and the reaction mixture is then stirred for 2 h. The solid is collected by centrifugation and washed with methanol and water, then dried under vacuum at 60 °C for 12 h, thus giving the desired thiol functionalized MIL-101 (Cr) -SH.<sup>3</sup>

#### *A-2.5. Synthesis of $[Zr_6O_4(OH)_4](bdc)_6$ (UiO-66)*

UiO-66 was synthesized according to a reported procedure.<sup>5</sup>  $ZrCl_4$  (125 mg, 0.54 mmol) was ultrasonically dissolved in a mixture of 15 mL DMF and 1 mL conc. HCl. 1,4-benzenedicarboxylic acid was then added to the solution which was sonicated for another 10 minutes. The resulting solution was placed in a 80 °C oven for 24 hours. The solid powder was obtained by filtration and washed with DMF.

#### *A-2.6. Synthesis of Au/MOFs materials*

An ethanolic solution (2 mL) containing MOF (20 mg) and the gold salt precursor  $HAuCl_4 \cdot 3H_2O$  (10 mg,  $2.5 \cdot 10^{-5}$  mol) was stirred under UV-visible irradiation (UV Rayonet system:  $\lambda = 253.7, 300, 350$  and  $575$  nm, 224 Watts, 1 h 30). The resulting solution was centrifuged at 6000 rpm during 3 min and the colorless supernatant was removed. The resulting powder was dried under the vacuum of a Schlenk line (1 h).

#### *A-2.7. Titanium doping on MOF-808-SH*

MOF-808-SH (60 mg) was activated at 150°C during 1h under controlled atmosphere. Then, a toluene solution of TiCl<sub>4</sub> (9.3 μL in 2 mL) was added and the resulting mixture was stirred during 30 min until an orange solution was obtained.<sup>6</sup> Anhydrous toluene was added (1 mL) and the mixture was centrifuged at 8000 rpm during 3 min under inert atmosphere. The supernatant was removed and 3 mL of anhydrous toluene was added in the resulting powder for a new centrifugation cycle (8000 rpm, 3 min). Finally, the colorless supernatant was removed and the resulting pale-yellow powder was dried under vacuum (100 mTorr) during 1 h.

## SECTION B – CHARACTERIZATION TECHNIQUES

$N_2$  adsorption-desorption isotherms studies were performed in a Quantachrome Autosorb IQ adsorption apparatus at 77 K and at pressure up to 1 bar after the samples (20 mg) were first degassed at 80 °C during 30 min and then at 120 °C during 3 h. The Brunauer-Emmett-Teller (BET) surface area was calculated using the adsorption data (Barret-Joyner-Halenda (BJH) method) in a relative pressure ranging from  $2 \cdot 10^{-6}$  to 1. The pores sizes were calculated by the Density Functional Theory (DFT) method using the adsorption branch of the isotherm. High resolution transmission electronic microscopy (HRTEM) observations were realized on a JEM-ARM200F with a cold field emission gun (guaranteed resolution at 78 picometers, energy resolution of 3 eV). A drop of a toluene suspension of the samples was deposited on a copper grid before microscopic observations. The diffuse reflectance spectra were recorded with a Agilent Cary 5000 UV-vis spectrometer using an integration sphere (specular mode) in the wavelength region: 200-800 nm. The powders were deposited on a glass slide covered by polytetrafluoroethylene (previously used as reference) before the measurements. For more understanding, the diffuse reflectance spectra were converted into absorption spectra. The x-ray photoelectron spectroscopy (XPS) analyses were performed in an ESCALAB 250 X-Ray photoelectron spectrometer, using Mg  $K\alpha$  X-Ray as the excitation source and a concentric hemispherical electron energy analyzer under high vacuum ( $10^{-9}$  mbar). The samples (powders) were deposited and pressed on a tungsten mesh (wires/In.: 100 x 100; wire diameter: 0.001"; width opening: 0.0090") prior to the analyses. Due to the insulating property of the samples, a neutralizer was used during the analyses (1  $\mu$ A). Low energy ions scattering (LEIS) measurements were performed under ultrahigh vacuum using a system equipped with an IonTOF Otac double-torroidal analyzer, using 3 keV  $He^+$  ions incident parallel to the sample normal. The analyzer geometry is such that all ions scattered through an annular region corresponding to a scattering angle of  $145^\circ$  are detected.  $Ar^+$  sputtering was

performed using 8 keV Ar<sup>+</sup> at normal incidence. The infrared absorption spectra were recorded with a Thermo-Nicolet FTIR. The samples (~2 mg of powder) were pressed onto KBr pellets and placed into a high-pressure high-temperature cell at the focal point of the sample compartment of the infrared spectrometer. The cell was connected to a vacuum-line for evacuation (base pressure ~100 mTorr). The samples were activated at 120°C under vacuum during 1 h to fully removed the pre-adsorbed water. The final spectra were recorded in transmission between 4000 cm<sup>-1</sup> and 400 cm<sup>-1</sup> (4 cm<sup>-1</sup> spectral resolution) with a MCTA detector under vacuum at 30 °C. The Raman analyses were performed on a Nicolet Almega XR Raman Spectrometer equipped with a 780 nm laser. The energy dispersive X-ray spectrometry (EDS) spectra were recorded on a Zeiss supra 40 scanning electron microscope (SEM) with an imaging resolution of 1-2 nm and with an EDAX X-ray spectrometer. The hydrogen production was measured by a Perkin-Elmer Clarus 580 gas chromatograph (GC) (PlotQ column (30 m) and PE-molisieve column (30 m)), TCD, vector gas: argon). Typically, 10 mg of photocatalyst was stirred into a quartz reactor with 10 mL of an aqueous solution of triethanolamine (TEOA) (1.10<sup>-2</sup> mol.L<sup>-1</sup>), purged with Argon during 2h and then pressurized at 1.2 bars. Finally, the reactor is irradiated at room temperature with a solar simulator (Xenon lamp, 300 Watts) equipped with a liquid lightguide (Lumatec®, series 380, 8 mm x 150 mm, from the near UV to the far red) during 66 h.

## SECTION C – EXPERIMENTAL MEASUREMENTS AND THEORETICAL MODELING

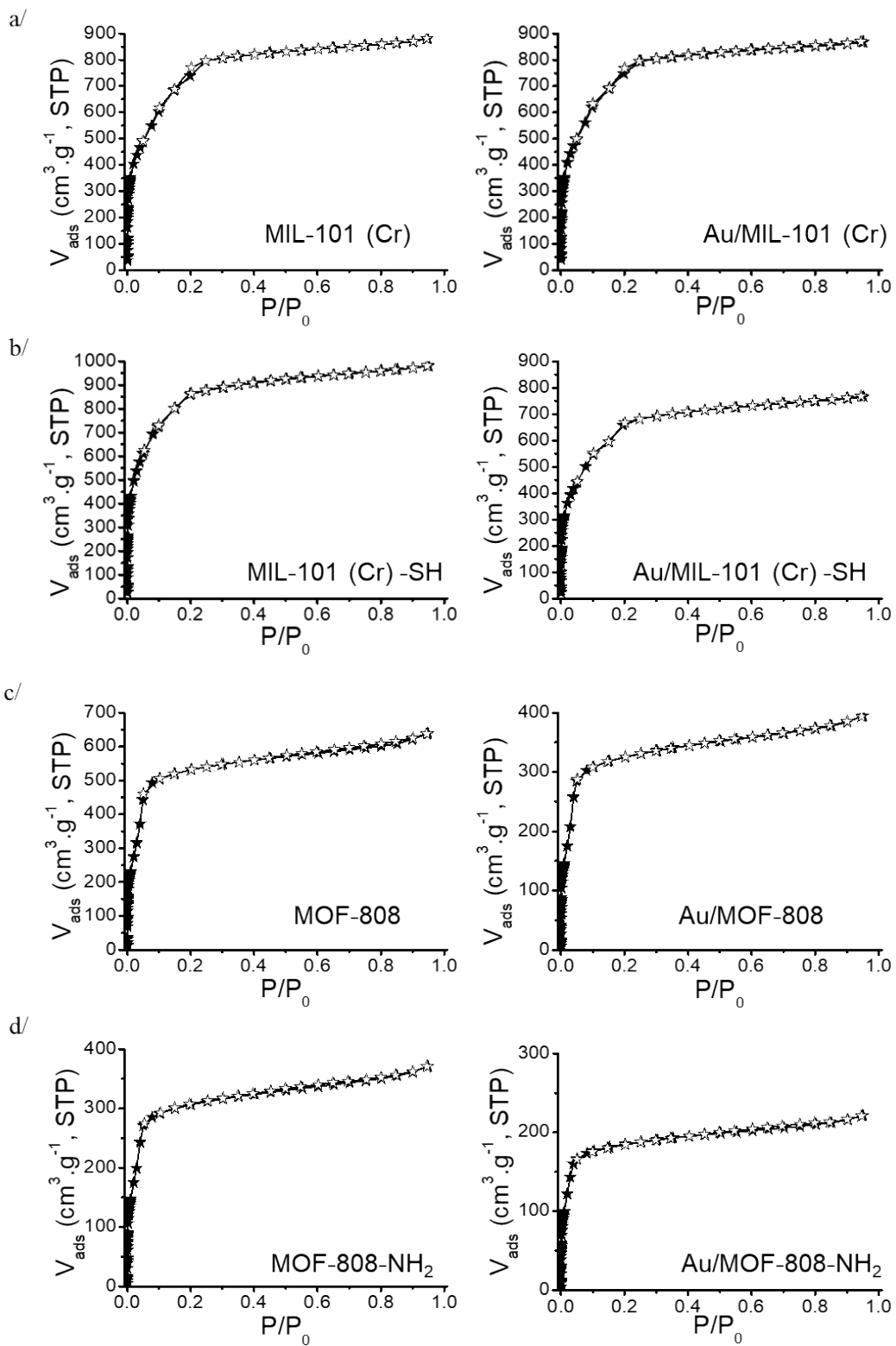
### C-1. Brunauer-Emmett-Teller (BET) results of Au/MOFs and MOFs materials

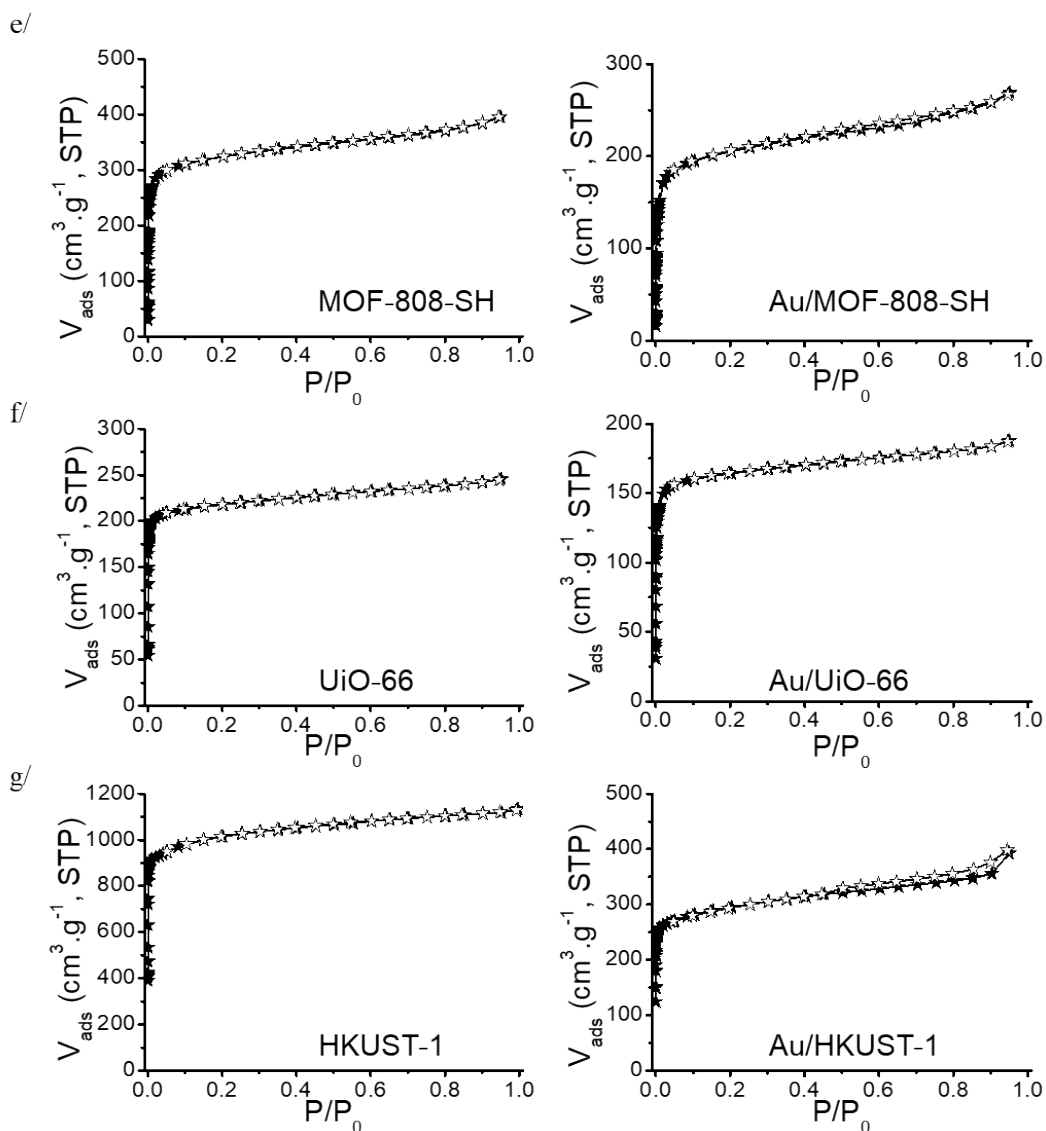
MOF-808 can be functionalized by amino or thiol functional groups in following a post-synthetic route to graft the corresponding paba (MOF-808-NH<sub>2</sub>) or pmba (MOF-808-SH) groups. The synthesis is described in the section A-2.2 of the SI. For completeness and to understand the effect of the pores sizes and the role of functionalized -SH groups on the Au NPs growth, three well-known MOFs are also studied: MIL-101 (Cr) and its functionalized form MIL-101 (Cr) -SH, UiO-66 and HKUST-1. The structural window and pore sizes, obtained from the measured or simulated crystallographic structures (Figure 2a, e, Figure S3), are listed in Table 1.<sup>1, 7-9</sup> For MIL-101 Cr -SH, the structural window and pore sizes could not be found in the literature.<sup>3</sup> For all the MOFs, the BET measurements (adsorption-desorption isotherms) are recorded before and after the Au NPs growth (Figure S1) and the pore sizes are calculated by Density Functional Theory (DFT) method using the measured adsorption isotherms of both the initial MOFs and modified Au/MOFs materials (Figure S2).

After Au NPs incorporation by photo-reduction of HAuCl<sub>4</sub> salt, surface area losses of 22%, 33%, 26%, 36%, 24%, 64% are measured, respectively, for MIL-101 (Cr) -SH, MOF-808, MOF-808-NH<sub>2</sub>, MOF-808-SH, UiO-66 and HKUST-1. The only exception is MIL-101 (Cr) for which the surface area increases by 2% after Au NPs incorporation, probably due to a weak fill rate of the pores by gold (Table 1). Note that a decrease of more than 50% is observed for HKUST-1, related to the fact that the Au NPs can close the opening windows and thus decrease the BET surface area since gas molecules cannot access the pores anymore. As expected if Au NPs are synthesized inside the pores, a decrease of  $dV/d\log(w)$  is observed for all the Au/MOFs (compared to the corresponding gold-free reference MOFs). Although these data are not sufficient to determine which pores are preferentially filled (largest or

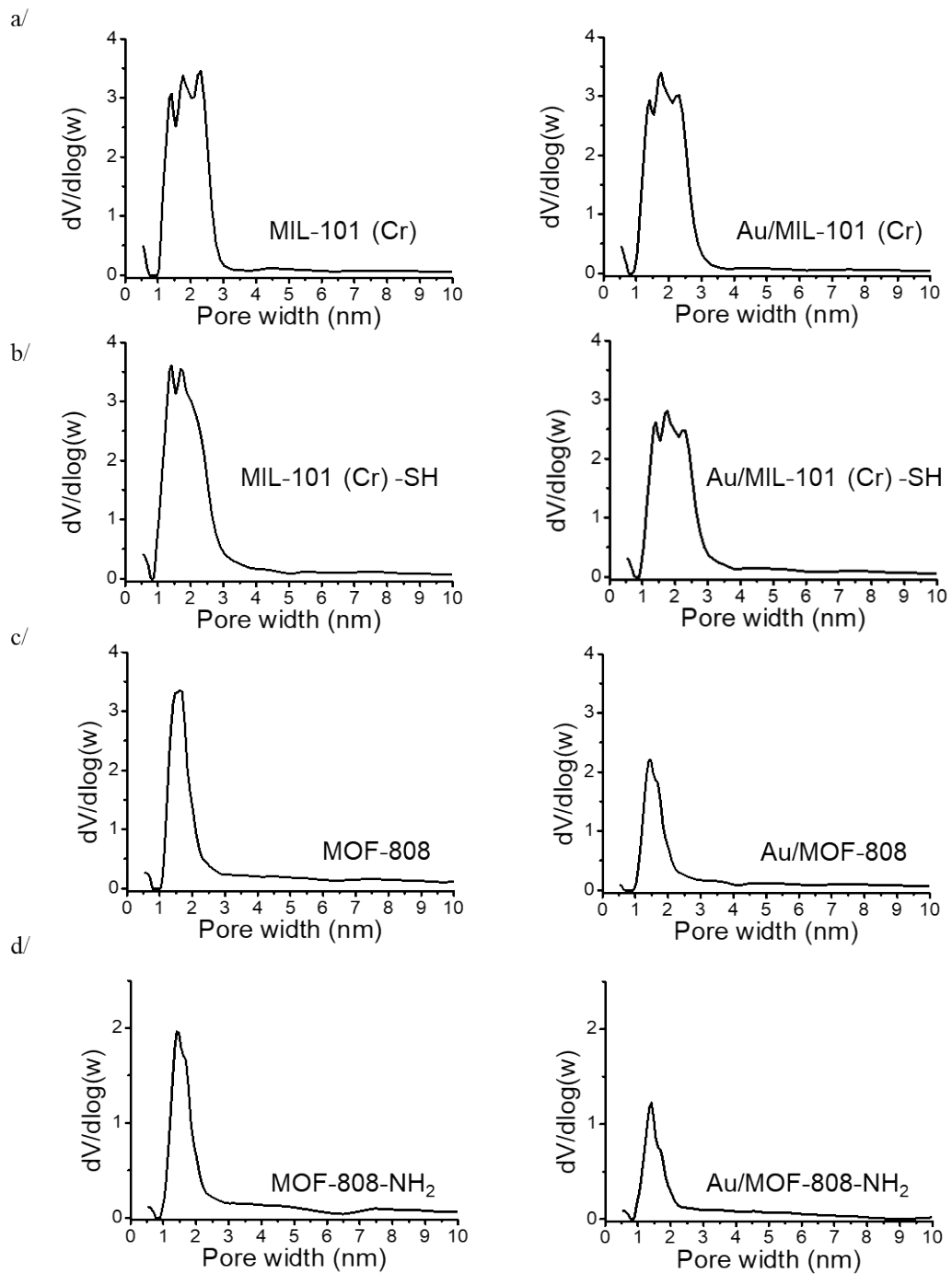
smallest) within the unit cell (Figure S2). However, the pore volumes all decrease after Au loading, which is expected after filling part of the pores with gold (Table 1).

These results are consistent with a confinement of Au NPs within MOFs since the inclusion of metal nanoparticles inside the pores and/or on the pore openings reduces the exchange of gas molecules between the core of the porous materials and the external environment.<sup>10</sup> The confinement of Au inside the pores is further supported by spectroscopic characterization (LEIS, IR, Raman) and *ab initio* calculations.





**Figure S1.** Nitrogen adsorption (full stars) and desorption (empty stars) isotherms measured at 77 K for the Au/MOF (right column) and MOF (left column) materials: (a) MIL-101 (Cr); (b) MIL-101 (Cr) -SH; (c) MOF-808; (d) MOF-808-NH<sub>2</sub>; (e) MOF-808-SH; (f) UiO-66; (g) HKUST-1.



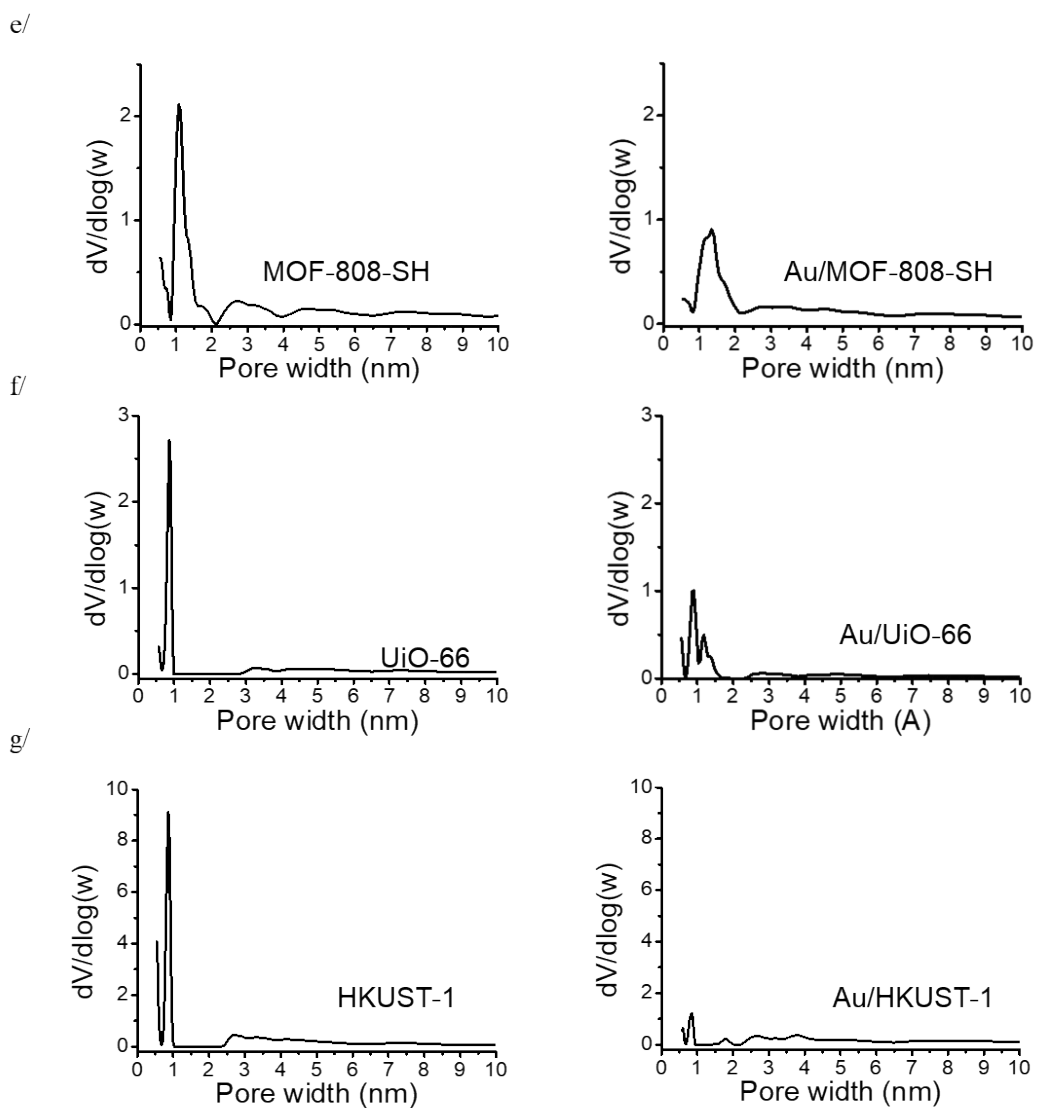


**Figure S2.** Mesopore size distributions for the Au/MOF (right column) and MOF (left column) materials calculated from the density functional theory model for: (a) MIL-101 (Cr); (b) MIL-101 (Cr) -SH; (c) MOF-808; (d) MOF-808-NH<sub>2</sub>; (e) MOF-808-SH; (f) UiO-66; (g) HKUST-1.

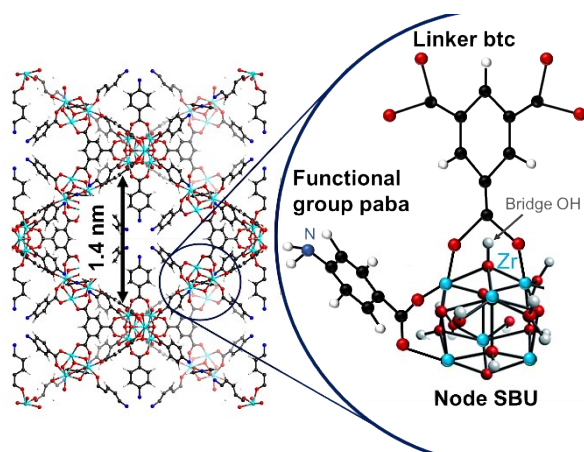


**Figure S3.** Crystallographic structure of the host MOF-808-NH<sub>2</sub> from modelling (insert: a schematic representation of the core of the pore). The structural pore size is 1.4 nm.

## C-2. HRTEM observations of Au/MOFs materials

### C-2.1. Au NPs mean diameters measurements

The HRTEM observations of Au/MOFs show the presence of Au NPs only in close proximity to the MOFs crystals (i.e. on the MOF surface or inside the MOF crystals) since no Au NPs are observed outside the MOF crystals (Figure 2b, f, Figure S4). From the HRTEM pictures, the mean diameters are measured:  $4.8 \pm 2.3$  nm;  $1.0 \pm 0.2$  nm;  $7.9 \pm 3.6$  nm;  $7.1 \pm 3.6$  nm;  $1.0 \pm 0.5$  nm;  $3.4 \pm 0.7$  nm and  $3.3 \pm 0.9$  nm, respectively for Au/MIL-101 (Cr), Au/MIL-101 (Cr) -SH, Au/MOF-808, Au/MOF-808-NH<sub>2</sub>, Au/MOF-808-SH, Au/Uio-66 and Au/HKUST-1 (Figure S4). Fast Fourier transform analyses of the pictures reveal that the Au NPs are crystalline in all cases since we observe Au (111) planes (Figure S4), which is typical for Au<sup>0</sup> NPs. Despite the large pores sizes of MIL-101 (Cr) -SH ( $1.4 \pm 0.1$  nm), only small Au NPs with a weak size dispersion at this scale ( $1.0 \pm 0.2$  nm) are observed, which is consistent with a strong stabilization of Au NPs by the thiol groups.

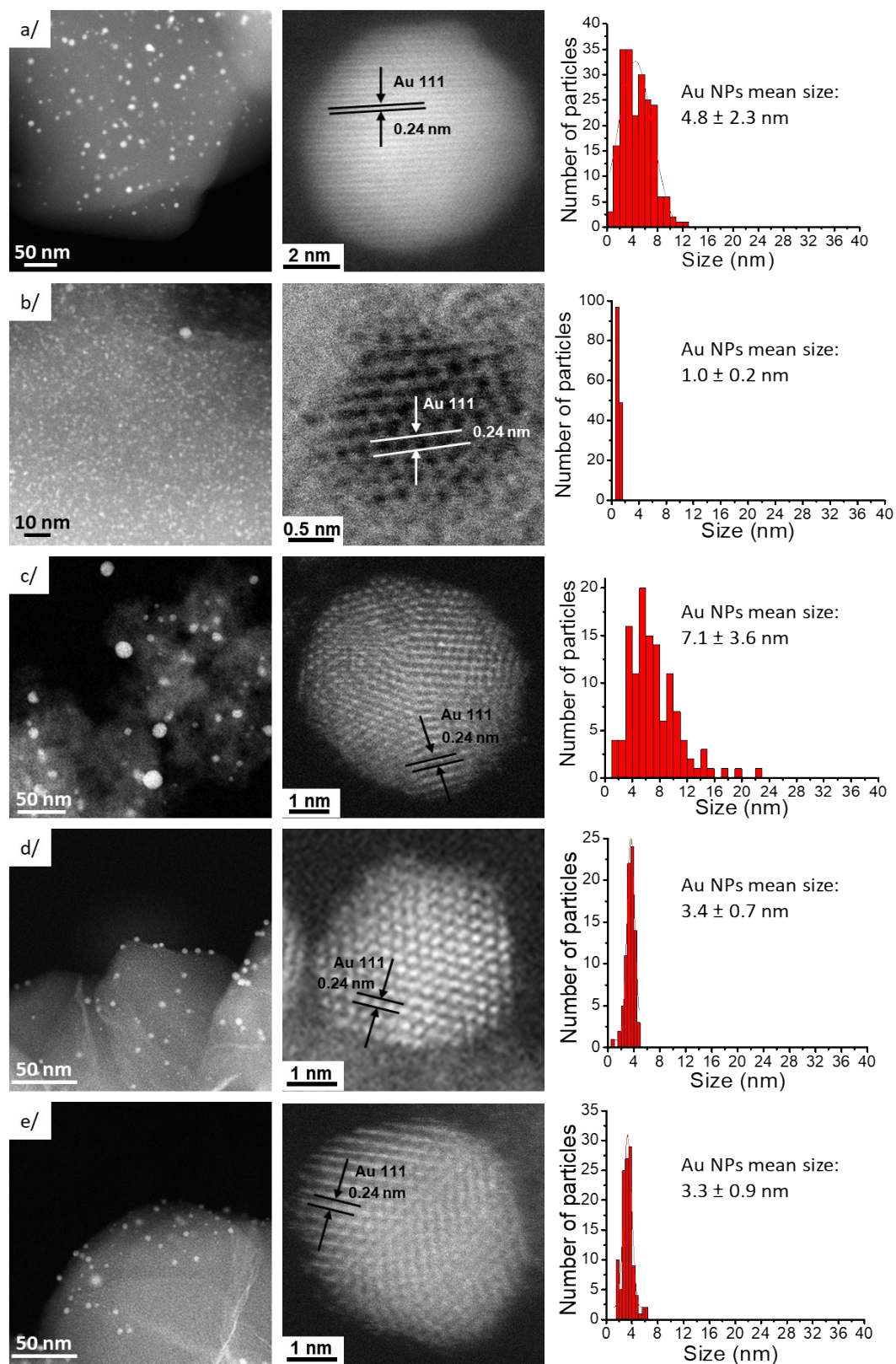


**Figure S4.** HRTEM observation of the Au/MOF materials (left column); crystalline Au NPs (middle column) and size dispersion of Au NPs (right column) for (a) MIL-101 (Cr); (b) MIL-101 (Cr) -SH; (c) MOF-808-NH<sub>2</sub>; (d) UiO-66; (e) HKUST-1.

*C-2.2. Correlation between the Au NP diameters and the pores widths in the MOF-808 series*

In the MOF-808 series, MOF-808-NH<sub>2</sub> and MOF-808-SH possess a relatively close pore width:  $1.4 \pm 0.1$  nm and  $1.07 \pm 0.05$  nm, respectively, and the same structural windows size: 0.5 and 0.35 nm (Table 1) and are therefore good hosts to study the influence of the functional groups only on the nanoparticle morphology. A modification of the Au NPs size appears as a function of the functional chemical groups:  $7.9 \pm 3.6$  nm (no functional groups),  $7.1 \pm 3.6$  nm (-NH<sub>2</sub>) and  $1.0 \pm 0.5$  nm (-SH) (Figure 2b, f, Figure S4c). Similar sizes of Au NPs are measured for Au/MOF-808 and Au/MOF-808-NH<sub>2</sub>, in contrast to MOF-808-SH, which shows that -NH<sub>2</sub> does not provide stabilization. On the other hand, the thiol groups impact the Au NPs size by stabilizing the Au within the confines of the pores.

Note that the equation (1) (Figure S5) is used to calculate the number of Au atoms contained in a spherical nanoparticle of 1 nm. The equation (2) is derived from the Wigner Seitz model and is applied to calculate the Wigner-Seitz radius  $R_s$ . The equation (3) gives the number of Au atoms on the surface of a spherical nanoparticle with a radius  $R$ .<sup>11</sup>

$$(1) N_{Vol} = (4/3 \cdot \pi \cdot R^3 \cdot d \cdot N_A) / M$$

$$(2) R_s = ((3 \cdot M) / (4/3 \cdot \pi \cdot d \cdot N_A))^{1/3}$$

$$(3) N_{surf} = N_{Vol} \cdot (6 \cdot R_s / R)$$

**Figure S5.** Equations for the calculation of the number of Au atoms in one Au spherical nanoparticle, with:  $N_{Vol}$ : number of Au atoms contained in the Au nanoparticle;  $N_{Surf}$  = number of Au atoms at the surface of the Au nanoparticle;  $R$ : radius of Au NPs (1 nm);  $d$ : density of gold ( $19.60 \text{ g}\cdot\text{cm}^{-3}$ );  $M$ : molecular weight of gold ( $196.97 \text{ g}\cdot\text{mol}^{-1}$ );  $N_A$ : number of Avogadro  $6.02 \times 10^{23}$ ;  $R_s$ : Wigner-Seitz radius.

### *C-2.3. Correlation between the Au NP diameters and the pores widths of the host MOFs*

The NP mean diameters are larger than the pores widths of the host MOFs, except for Au/MOF-808-SH and Au/MIL-101 (Cr) -SH, highlighting a strong stabilization of the Au NPs by thiol groups, since the Au NP mean diameter ( $1.0 \pm 0.5$  nm and  $1.0 \pm 0.2$  nm, respectively) is in accordance with (or even a bit smaller than) the pores width for MOF-808-SH ( $1.07 \pm 0.05$  nm) and MIL-101 (Cr) -SH ( $1.4 \pm 0.1$  nm). A correlation can be established between the Au NPs mean diameter and the pores sizes of the MOFs without functional chemical groups (MIL-101 (Cr), MOF-808, UiO-66 and HKUST-1): the metal nanoparticles size decreases with the pore size width and the windows size (Table 1). The pore volumes therefore act as nano-reactors for the creation and stabilization of metal nanoparticles but the confinement effect of pores is not sufficient to avoid a growth of the nanoparticles beyond the pore walls, leading to aggregation inside the pores channels, as previously reported by Esken, D. *et al.*: Au NP occupying 4 ZIF cavities in Au/ZIF-8 material and explained by Garcia H. *et al.*<sup>10, 12</sup> Indeed, sonication clearly affects the Au NP mean diameters as detailed in the next section (C-2.4) of the SI.

### *C-2.4. Effects of ultrasounds on the Au NPs mean size*

After 2 minutes of sonication in toluene, HRTEM pictures show that the Au NPs diameters and size dispersions increase for Au/MIL-101 (Cr) (from  $4.8 \pm 2.3$  nm to  $15.4 \pm 3.2$  nm), Au/UiO-66 ( $3.4 \pm 0.7$  nm to  $19.6 \pm 11.4$  nm) and Au/HKUST-1 ( $3.3 \pm 0.9$  nm to  $5.4 \pm 2.9$  nm) materials (Figure S6). Ultrasounds foster the contacts and aggregation between adjacent Au nanoparticles resulting in an increase of their sizes. Confinement by the MOFs is well established even if the Au NPs sizes are larger than the host MOFs pores, but it is not the only factor that can act on the Au NPs diameters.

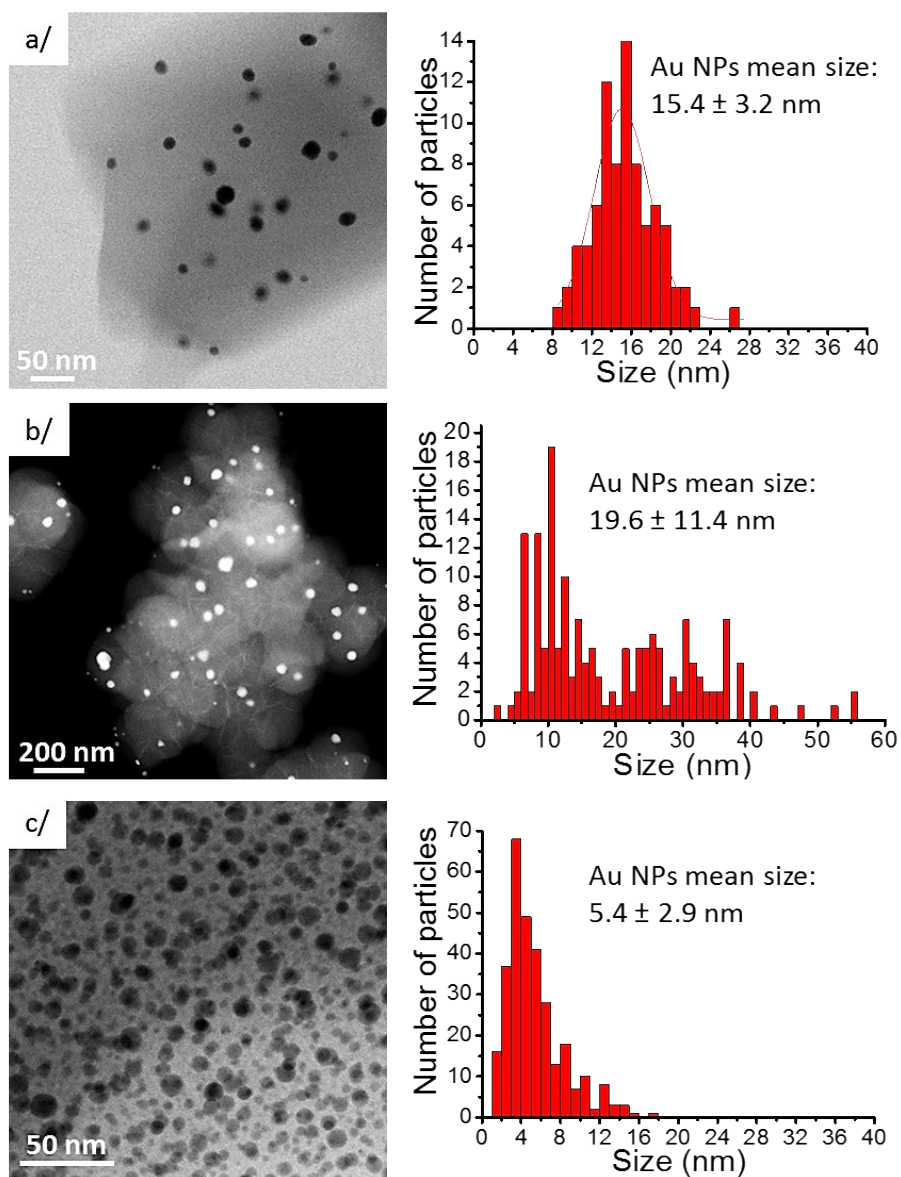


**Figure S6.** (a) HRTEM observations after application of ultrasounds during 5 minutes on Au/MIL-101 (Cr) ; (b) Au/UiO-66; and (c) Au/HKUST-1 materials.

*C-2.5. Stabilization of Au NPs in Au/MOF-808-SH after 9 months*

After a 9-month storage of Au/MOF-808-SH material under ambient conditions (air, atmospheric pressure, ambient humidity and temperature), the HRTEM observations (Figure S7) show that the size of Au NPs is maintained (~1 nm).

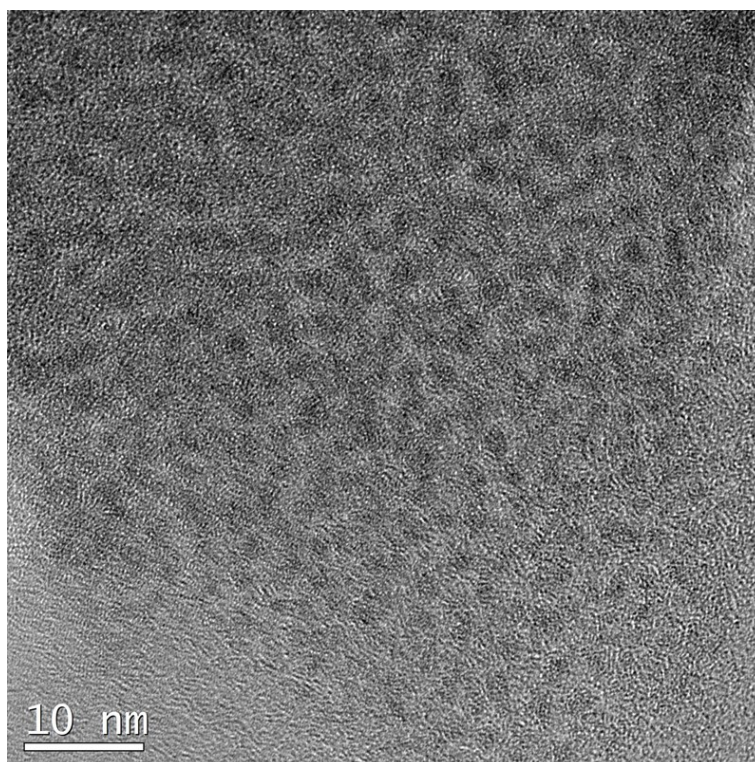


**Figure S7.** HRTEM observations of aged (9 months) Au/MOF-808-SH.

### C-3. XPS spectra of Au/MOFs and MOFs materials

For further analysis of the surface chemistry of Au/MOFs and MOFs materials, XPS characterization is performed (Figure S8 to S14). The sensitivity to the binding energies of electrons of an atom to the local electronic state of adjacent atoms provides information on binding, coordination or interaction between chemical groups. Here, as the MOF materials used are very insulating, charging effects can induce shifts affecting all the spectral regions, despite the use of a charges neutralizer (Table S1 to S8), which makes the interpretation more difficult. Note that MIL-101 (Cr) -SH is particularly insulating and a huge charging effect is observed. Nevertheless, in Au/MIL-101 (Cr) -SH, the Au 4f<sub>7/2</sub>, Au 4f<sub>5/2</sub> and S 2p contributions are observed, providing further evidence that thiol groups and Au<sup>0</sup> are present in the material in accordance with the observation of reduced Au NPs by HRTEM (Figure S4b).

For example, in the Au/MOF-808 (Figure S10) and Au/MOF-808-SH (Figure S12) spectra, the C 1s spectrum is characterized by two components obtained by deconvolution, respectively located at 293.1 eV and 289.3 eV and at 290.7 eV and 286.8 eV for MOF-808 and MOF-808-SH. These peaks are assigned respectively to the carboxylate groups (COO) and the adventitious carbons (C-C, C-H) of the linker btc. The deconvoluted Zr 3d spectrum consists of two peaks located at 188.6 eV and 186.2 eV for Au/MOF-808 and at 184.9 eV and 182.6 eV for Au/MOF-808-SH and are assigned respectively to Zr 3d<sub>3/2</sub> and Zr 3d<sub>5/2</sub>. Finally, in the Au 4f binding energies region, two Au peaks are detected at 92.8 eV and 89.2 eV in Au/MOF-808 and at 89.6 eV and 86.0 eV in Au/MOF-808-SH (Figure S10e, Figure S12f). They correspond respectively to the Au 4f<sub>5/2</sub> and Au 4f<sub>7/2</sub> contributions ( $\Delta E(\text{Au } 4f_{7/2} - \text{Au } 4f_{5/2}) = 3.6 \text{ eV}$  for all the MOFs), providing further evidence that Au<sup>0</sup> is present in the samples in accordance with the observation of reduced Au NPs by HRTEM (Figure 2b, f, Figure S4).<sup>13</sup> For all the others Au/MOF materials, only two contributions (Au 4f<sub>5/2</sub> and Au 4f<sub>7/2</sub>) are observed in the Au 4f binding energies region, again associated with reduced Au<sup>0</sup>. These XPS

observations correlated with the observations of crystalline Au<sup>0</sup> NPs by HRTEM and the appearance of a LSPR band on UV-vis spectra (Figure 2d, h) prove the reduction of the initial HAuCl<sub>4</sub> salt during the photo-reduction method (section C-2.1 and C-5, SI).

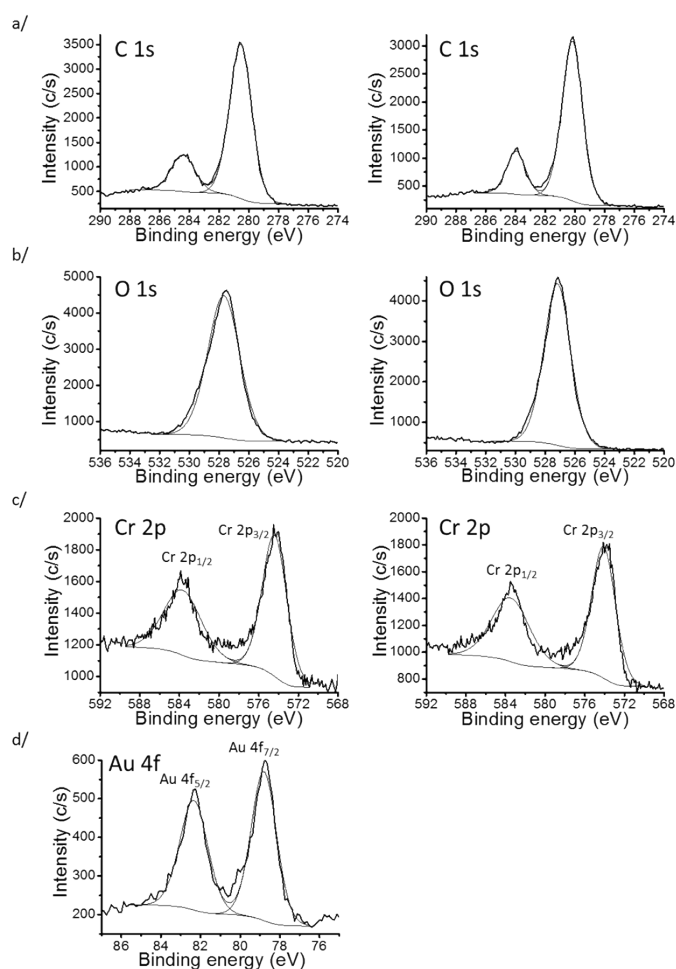


**Figure S8.** XPS spectra of Au/MIL-101 (Cr) (left column) and MIL-101 (Cr) (Cr<sub>3</sub>O(bdc)<sub>3</sub>F(H<sub>2</sub>O)<sub>2</sub>) (right column): (a) C 1s; (b) O 1s; (c) Cr 2p<sub>1/2,3/2</sub>; (d) Au 4f<sub>5/2,7/2</sub> regions.

**Table S1.** Main components positions ( $\pm 0.1$  eV), FWHM ( $\pm 0.05$  eV) for each element (C, O, Cr, Au) for Au/MIL-101 (Cr) and MIL-101 (Cr) materials.

	<b>C 1s</b>		<b>O 1s</b>	<b>Cr 2p</b>		<b>Au 4f</b>	
				<b>Cr 2p<sub>1/2</sub></b>	<b>Cr 2p<sub>3/2</sub></b>	<b>Au 4f<sub>5/2</sub></b>	<b>Au 4f<sub>7/2</sub></b>
<b>MIL-101 (Cr)</b>	284.0	280.2	527.2	583.5	574.1	-	-
	(1.5)	(1.6)	(2.1)	(3.3)	(2.7)	-	-
<b>Au/MIL-101 (Cr)</b>	284.4	280.6	527.7	583.7	574.4	82.3	78.8
	(1.9)	(1.8)	(2.5)	(3.4)	(2.6)	(1.7)	(1.5)

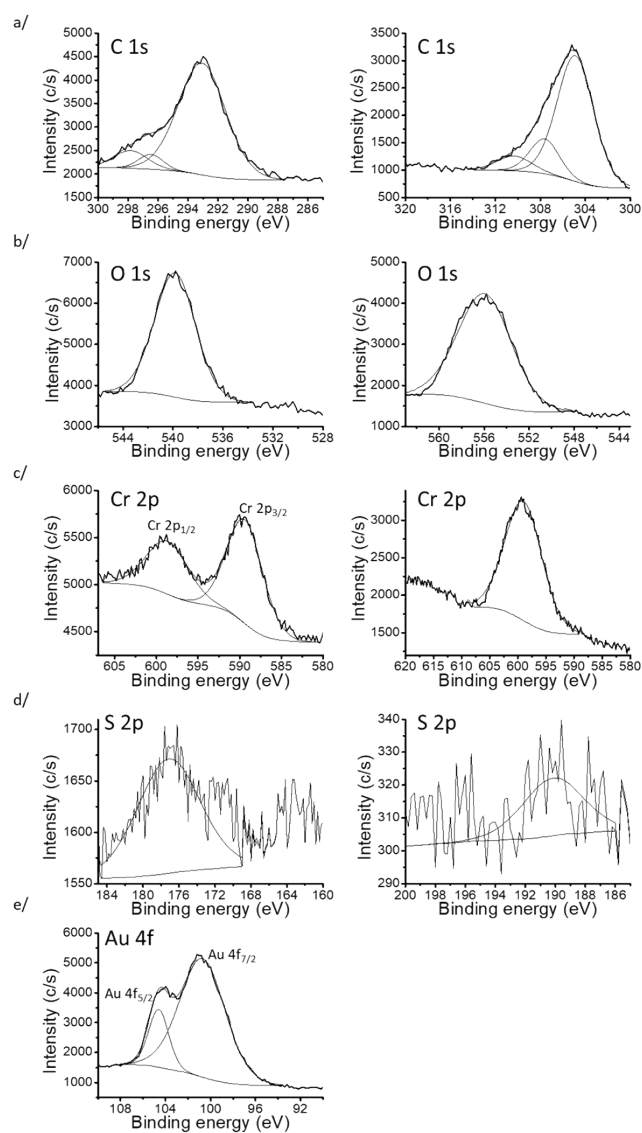


**Figure S9.** XPS spectra of Au/MIL-101 (Cr) -SH (left column) and MIL-101 (Cr) -SH (right column): (a) C 1s; (b) O 1s; (c) Cr  $2p_{1/2,3/2}$ ; (d) S 2p; (e) Au  $4f_{5/2,7/2}$  regions.

**Table S2.** Main components positions ( $\pm 0.1$  eV), FWHM ( $\pm 0.05$  eV) for each element (C, O, Cr, S, Au) for Au/MIL-101 (Cr) -SH and MIL-101 (Cr) -SH materials.

	C 1s			O 1s	Cr 2p <sub>1/2</sub>	Cr 2p <sub>3/2</sub>	S 2p	Au 4f	
	Au/MIL-101 (Cr) -SH	MIL-101 (Cr) -SH	MIL-101 (Cr) -SH	MIL-101 (Cr) -SH	MIL-101 (Cr) -SH	MIL-101 (Cr) -SH	MIL-101 (Cr) -SH	Au 4f <sub>5/2</sub>	Au 4f <sub>7/2</sub>
<b>MIL-101 (Cr) -SH</b>	310.3 (3.6)	307.6 (3.1)	304.9 (3.8)	555.9 (5.6)	- (-)	599.0 (7.7)	190.2 (4.80)	- (-)	- (-)
<b>Au/MIL-101 (Cr) -SH</b>	297.8 (2.7)	296.5 (1.9)	293.1 (3.7)	539.8 (3.9)	598.6 (5.9)	589.4 (5.1)	177.1 (8.2)	104.6 (4.8)	100.7 (2.1)

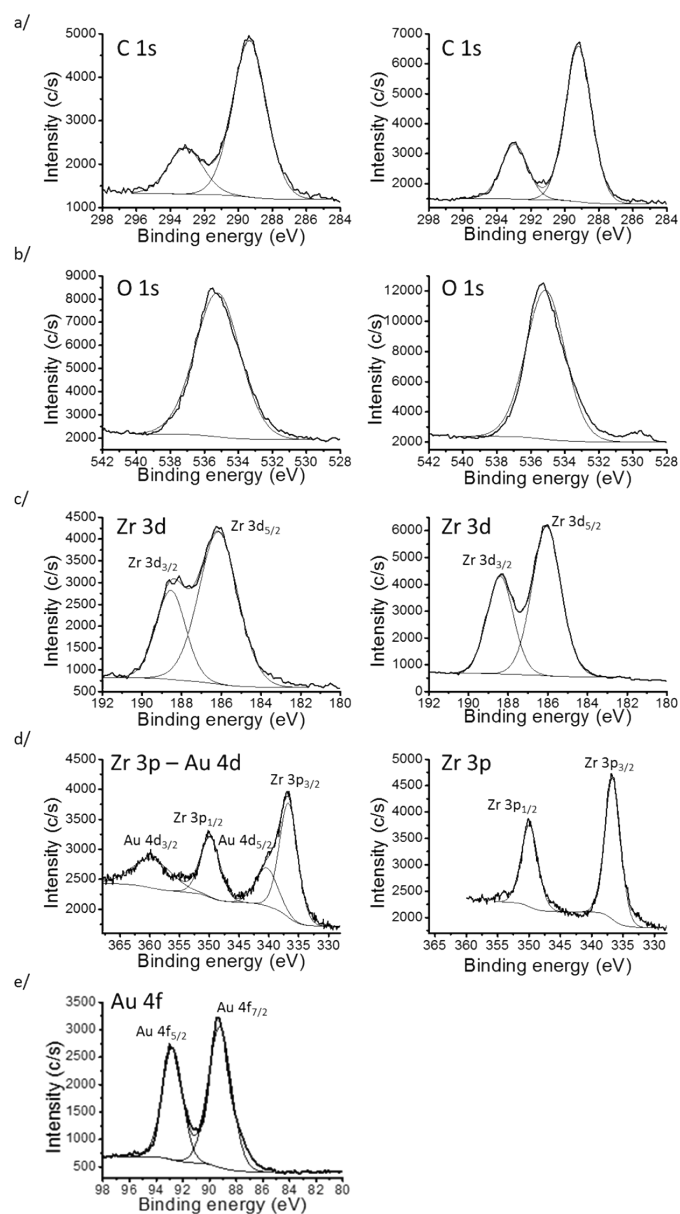


**Figure S10.** XPS spectra of Au/MOF-808 (left column) and MOF-808 ( $\text{Zr}_6\text{O}_4(\text{OH})_4(\text{H}_2\text{O}(\text{OH}))_6(\text{btc})_6$ ) (right column): (a) C 1s; (b) O 1s; (c) Zr  $3d_{3/2,5/2}$ ; (d) Zr  $3p_{1/2,3/2}$  – Au  $4d_{3/2,5/2}$ ; (e) Au  $4f_{5/2,7/2}$  regions.

**Table S3.** Main components positions ( $\pm 0.1$  eV), FWHM ( $\pm 0.05$  eV) for each element (C, O, Zr, Au) for Au/MOF-808 and MOF-808 materials.

	C 1s		O 1s	Zr 3p		Zr 3d		Au 4f		Au 4d	
				Zr 3p <sub>1/2</sub>	Zr 3p <sub>3/2</sub>	Zr 3d <sub>3/2</sub>	Zr 3d <sub>5/2</sub>	Au 4f <sub>5/2</sub>	Au 4f <sub>7/2</sub>	Au 4d <sub>3/2</sub>	Au 4d <sub>5/2</sub>
<b>MOF-808</b>	293.0	289.2	535.1	349.9	336.6	188.4	186.1	-	-	-	-
	(1.8)	(1.8)	(2.7)	(3.1)	(3.0)	(1.6)	(1.7)	-	-	-	-
<b>Au/MOF-808</b>	293.1	289.3	535.2	349.9	336.7	188.6	186.2	92.8	89.2	340.4	359.7
	(2.4)	(2.4)	(3.1)	(3.4)	(3.3)	(1.8)	(2.3)	(1.8)	(2.1)	(3.6)	(3.7)

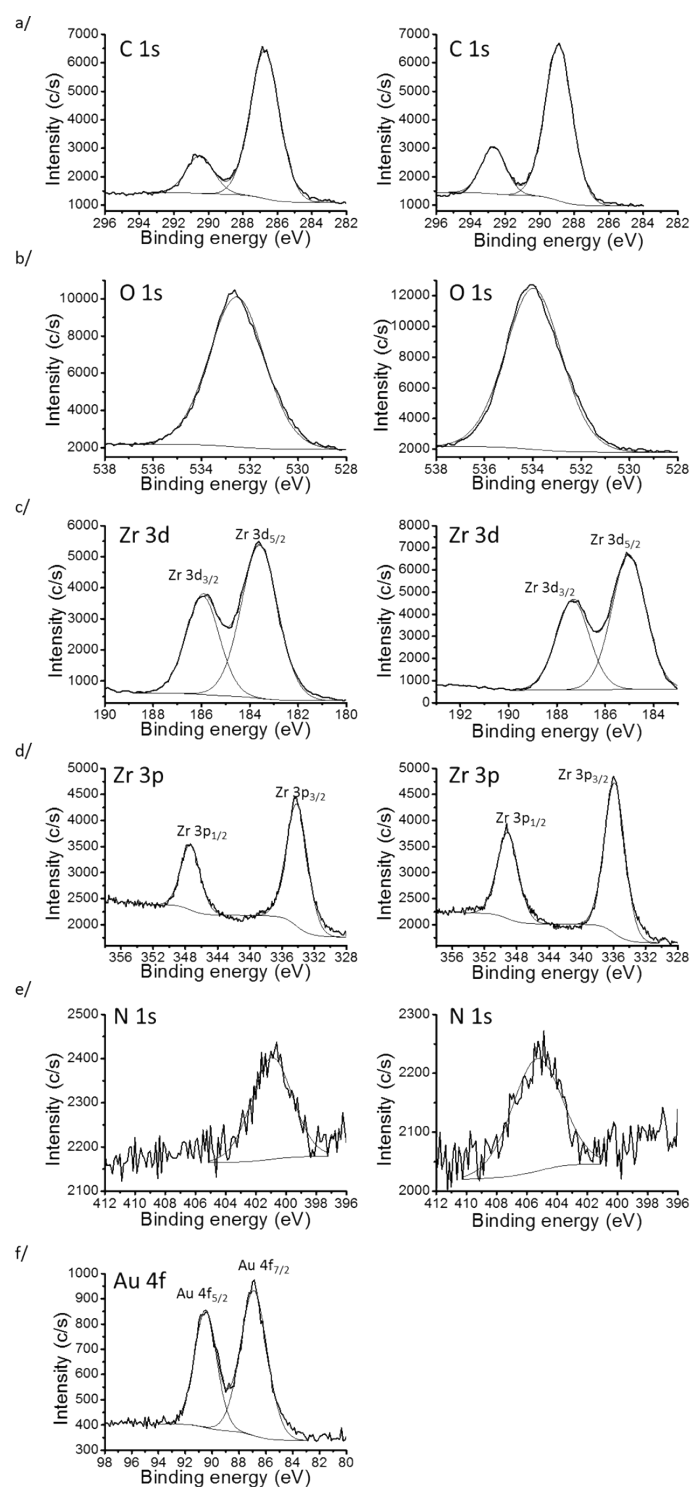


**Figure S11.** XPS spectra of Au/MOF-808-NH<sub>2</sub> (left column) and MOF-808-NH<sub>2</sub> (Zr<sub>6</sub>O<sub>4</sub>(OH)<sub>4</sub>(paba)<sub>6</sub>(btc)<sub>6</sub>) (right column): (a) C 1s; (b) O 1s; (c) Zr 3d<sub>3/2,5/2</sub>; (d) Zr 3p<sub>1/2,3/2</sub>; (e) N 1s; (f) Au 4f<sub>5/2,7/2</sub> regions.

**Table S4.** Main components positions ( $\pm 0.1$  eV), FWHM ( $\pm 0.05$  eV) for each element (C, O, Zr, N, Au) for Au/MOF-808-NH<sub>2</sub> and MOF-808-NH<sub>2</sub> materials.

	C 1s		O 1s	Zr 3p		Zr 3d		N 1s	Au 4f	
				Zr 3p <sub>1/2</sub>	Zr 3p <sub>3/2</sub>	Zr 3d <sub>3/2</sub>	Zr 3d <sub>5/2</sub>		Au 4f <sub>5/2</sub>	Au 4f <sub>7/2</sub>
<b>MOF-808-NH<sub>2</sub></b>	292.7	288.9	534.0	349.1	335.8	187.4	185.0	405.3	-	-
	(1.7)	(1.9)	(2.7)	(3.1)	(3.0)	(1.6)	(1.7)	(3.8)	-	-
<b>Au/MOF-808-NH<sub>2</sub></b>	290.5	286.7	532.5	347.4	334.1	186.0	183.6	400.9	90.5	86.9
	(1.9)	(2.0)	(2.7)	(3.0)	(3.0)	(1.6)	(1.8)	(3.2)	(2.0)	(2.3)

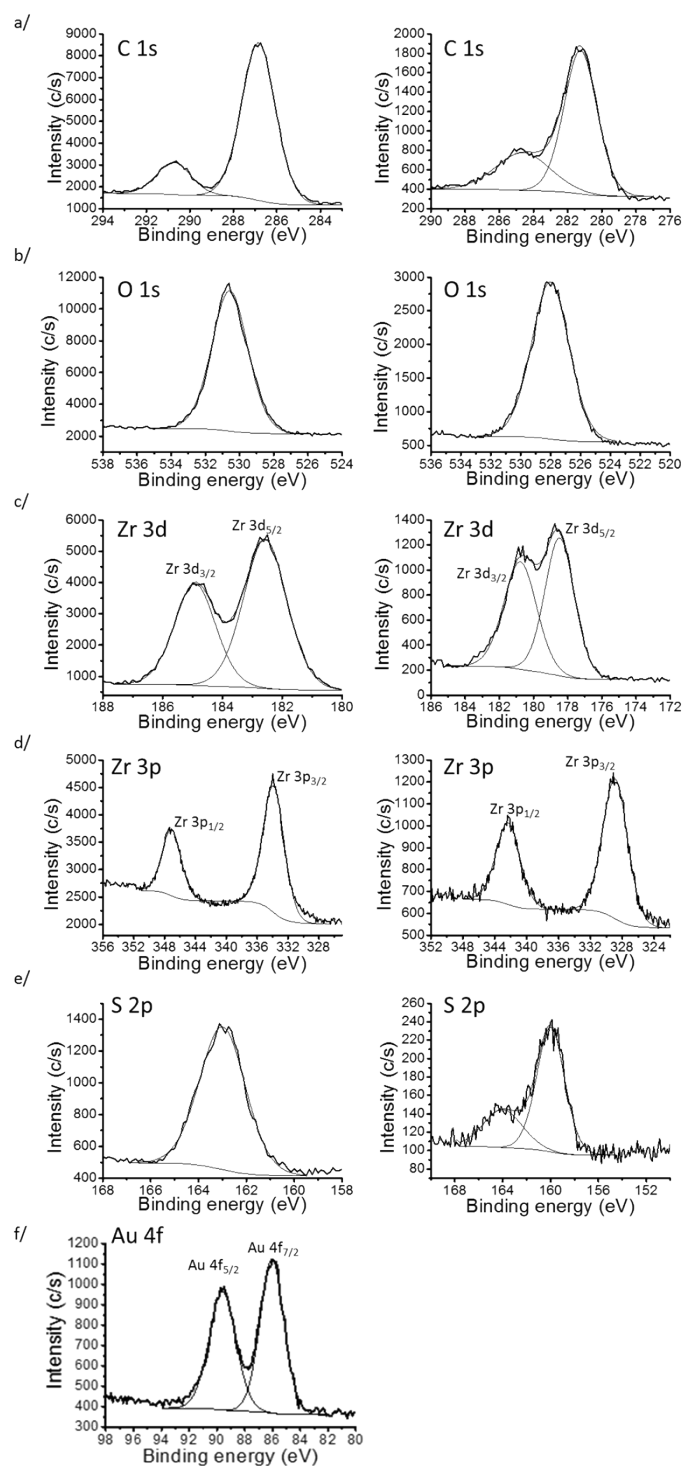


**Figure S12.** XPS spectra of Au/MOF-808-SH (left column) and MOF-808-SH ( $\text{Zr}_6\text{O}_4(\text{OH})_4(\text{pmba})_6(\text{btc})_6$ ) (right column): (a) C 1s; (b) O 1s; (c) Zr  $3d_{3/2,5/2}$ ; (d) Zr  $3p_{1/2,3/2}$ ; (e) S 2p; (f) Au  $4f_{5/2,7/2}$  regions.

**Table S5.** Main components positions ( $\pm 0.1$  eV), FWHM ( $\pm 0.05$  eV) for each element (C, O, Zr, S, Au) for Au/MOF-808-SH and MOF-808-SH materials.

	C 1s		O 1s	Zr 3p		Zr 3d		S 2p		Au 4f	
				Zr 3p <sub>1/2</sub>	Zr 3p <sub>3/2</sub>	Zr 3d <sub>3/2</sub>	Zr 3d <sub>5/2</sub>			Au 4f <sub>5/2</sub>	Au 4f <sub>7/2</sub>
<b>MOF-808-SH</b>	284.6	281.2	528.0	342.3	328.9	180.8	178.5	164.0	160.0	-	-
	(3.7)	(2.3)	(3.0)	(3.5)	(3.7)	(3.8)	(2.7)	(2.3)	(2.0)	-	-
<b>Au/MOF-808-SH</b>	290.7	286.8	530.6	347.1	333.9	184.9	182.6	163.0	-	89.6	86.0
	(1.8)	(1.8)	(2.5)	(2.9)	(3.3)	(1.6)	(1.7)	(2.3)	-	(2.3)	(2.0)

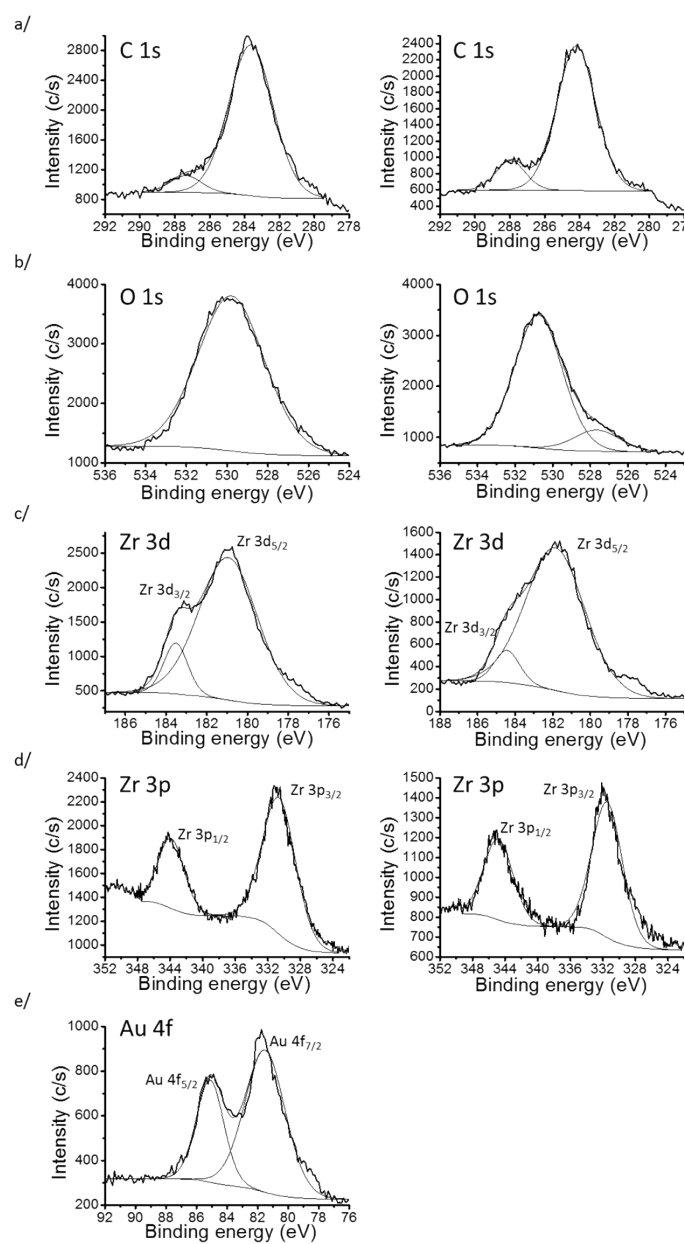


**Figure S13.** XPS spectra of Au/Uio-66 (left column) and Uio-66 (Zr<sub>6</sub>O<sub>4</sub>(OH)<sub>4</sub>(bdc)<sub>6</sub>) (right column): (a) C 1s; (b) O 1s; (c) Zr 3d<sub>3/2,5/2</sub>; (d) Zr 3p<sub>1/2,3/2</sub>; (e) Au 4f<sub>5/2,7/2</sub> regions.

**Table S6.** Main components positions ( $\pm 0.1$  eV), FWHM ( $\pm 0.05$  eV) for each element (C, O, Zr, Au) for Au/UiO-66 and UiO-66 materials.

	C 1s		O 1s		Zr 3p		Zr 3d		Au 4f	
					Zr 3p <sub>1/2</sub>	Zr 3p <sub>3/2</sub>	Zr 3d <sub>3/2</sub>	Zr 3d <sub>5/2</sub>	Au 4f <sub>5/2</sub>	Au 4f <sub>7/2</sub>
<b>UiO-66</b>	288.0	284.2	530.8	527.7	344.8	331.5	184.4	181.9	-	-
	(2.0)	(2.6)	(3.0)	(2.9)	(3.7)	(3.9)	(1.6)	(3.7)	-	-
<b>Au/UiO-66</b>	287.4	283.6	529.8	-	343.9	330.6	183.5	180.9	85.1	81.5
	(2.1)	(3.0)	(3.9)	-	(3.6)	(4.3)	(1.4)	(3.4)	(2.1)	(3.1)

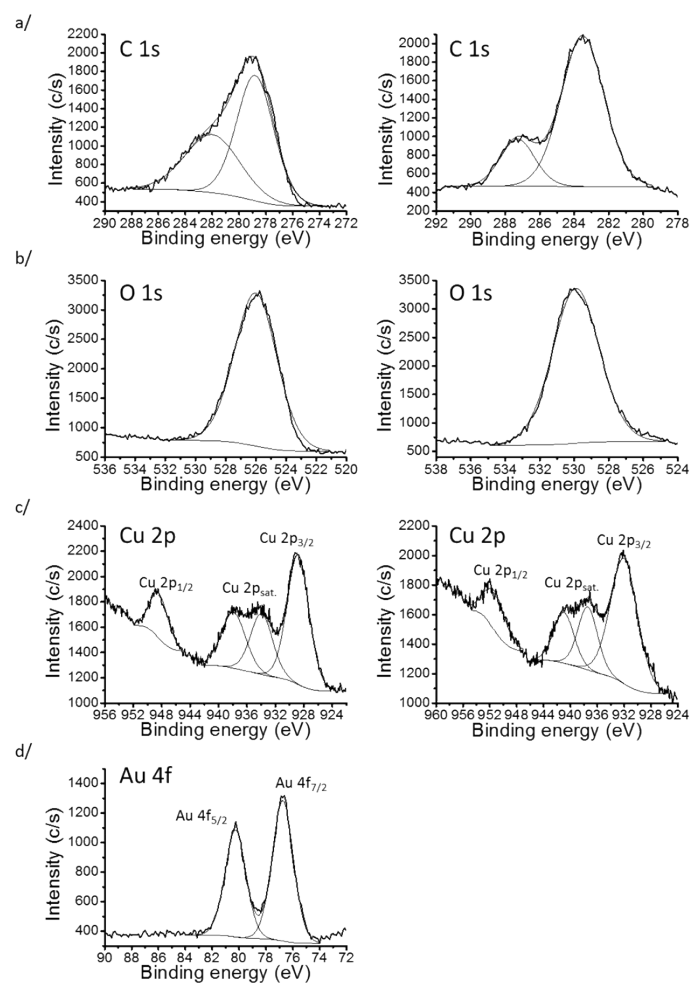


**Figure S14.** XPS spectra of Au/HKUST-1 (left column) and HKUST-1 (Cu<sub>3</sub>(bdc)<sub>2</sub>(H<sub>2</sub>O)<sub>3</sub>) (right column): (a) C 1s; (b) O 1s; (c) Cu 2p<sub>1/2,3/2</sub>; (d) Au 4f<sub>5/2,7/2</sub> regions.

**Table S7.** Main components positions ( $\pm 0.1$  eV), FWHM ( $\pm 0.05$  eV) for each element (C, O, Cu, Au) for Au/HKUST-1 and HKUST-1 materials.

	<b>C 1s</b>		<b>O 1s</b>	<b>Cu 2p</b>			<b>Au 4f</b>		
				<b>Cu 2p<sub>1/2</sub></b>	<b>Cu 2p<sub>sat.</sub></b>	<b>Cu 2p<sub>3/2</sub></b>	<b>Au 4f<sub>5/2</sub></b>	<b>Au 4f<sub>7/2</sub></b>	
<b>HKUST-1</b>	287.3	283.5	531.8	951.3	944.1	937.4	932.0	-	-
	(2.4)	(2.9)	(3.0)	(3.8)	(3.4)	(3.9)	(4.2)	-	-
<b>Au/HKUST-1</b>	281.9	278.8	526.0	948.4	937.9	933.9	928.8	80.3	76.7
	(4.5)	(3.2)	(3.3)	(3.1)	(3.8)	(3.7)	(3.6)	(1.8)	(1.8)

#### C-4. XRD diagrams of Au/MOF and MOFs materials

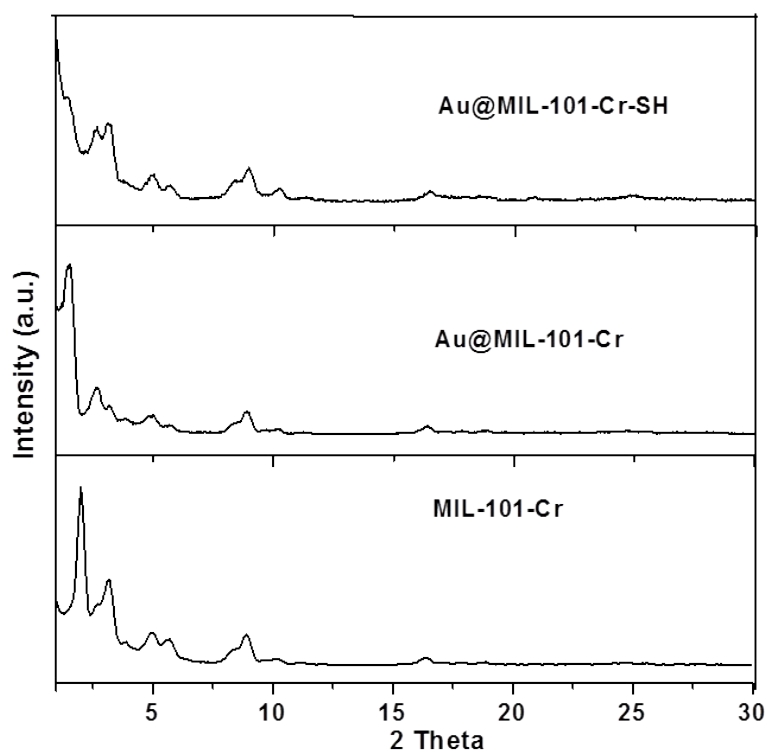


**Figure S15.** XRD diagrams of MIL-101-Cr, Au/MIL-101-Cr, and Au/MIL-101-Cr-SH.

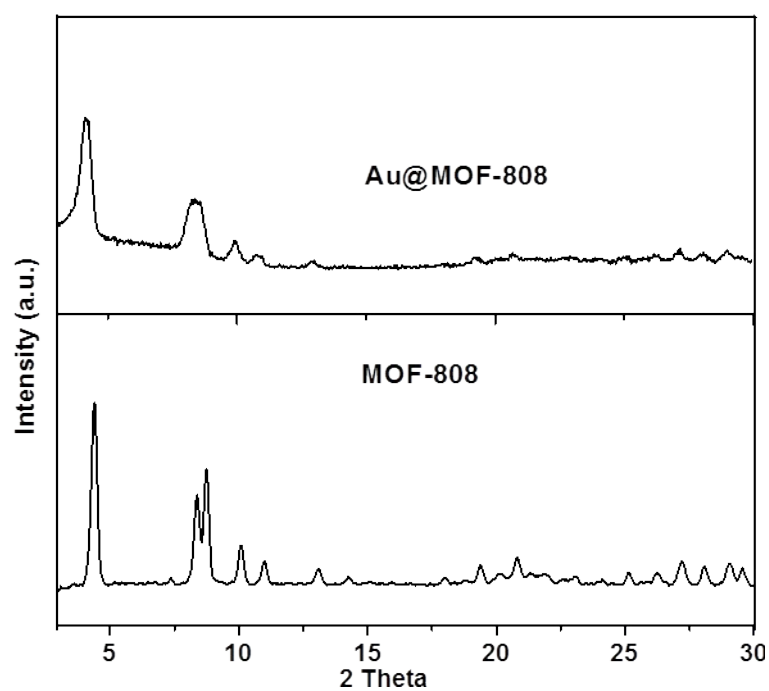


**Figure S16.** XRD diagrams of MOF-808 and Au/MOF-808.

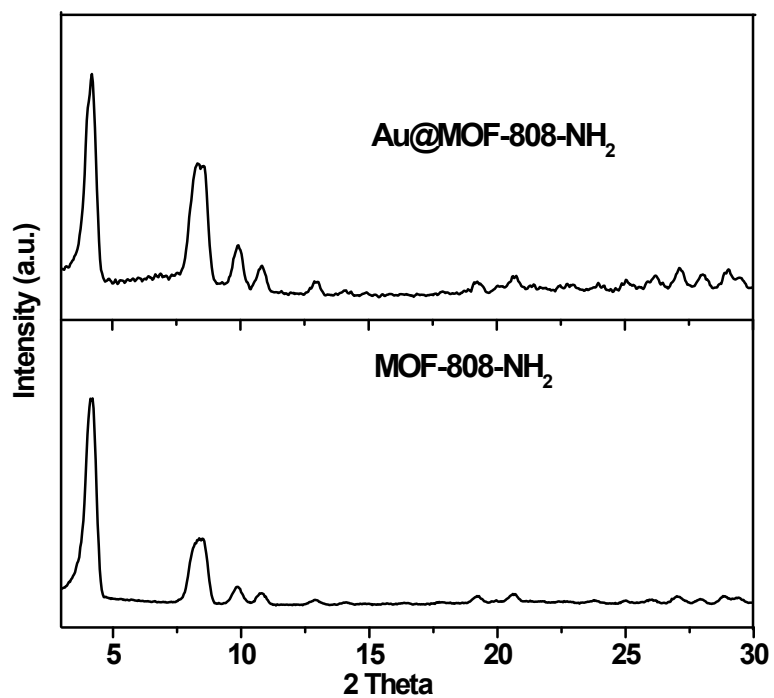


**Figure S17.** XRD diagrams of MOF-808-NH<sub>2</sub> and Au/MOF-808-NH<sub>2</sub>.

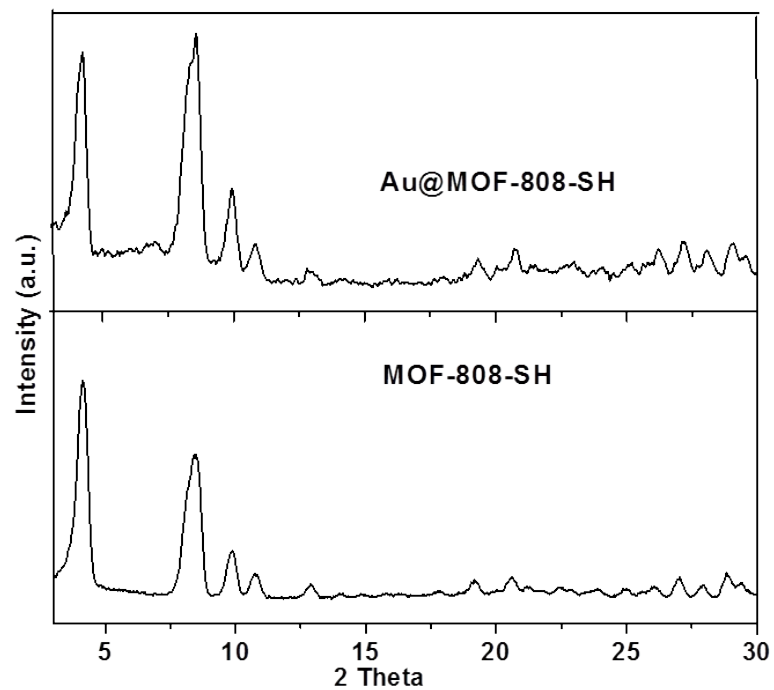


**Figure S18.** XRD diagrams of MOF-808-SH and Au/MOF-808-SH.

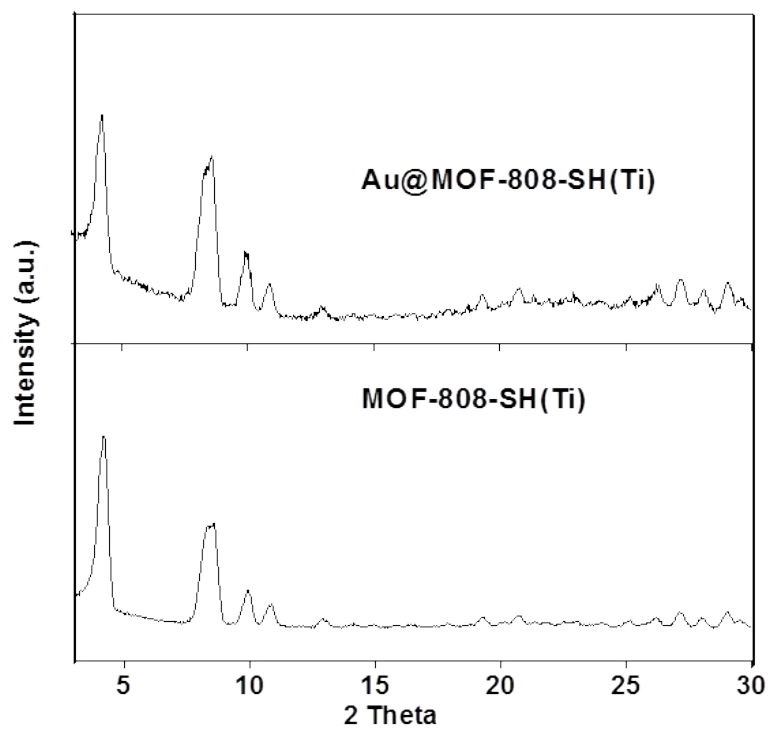


**Figure S19.** XRD diagrams of MOF-808-SH (Ti) and Au/MOF-808-SH (Ti).

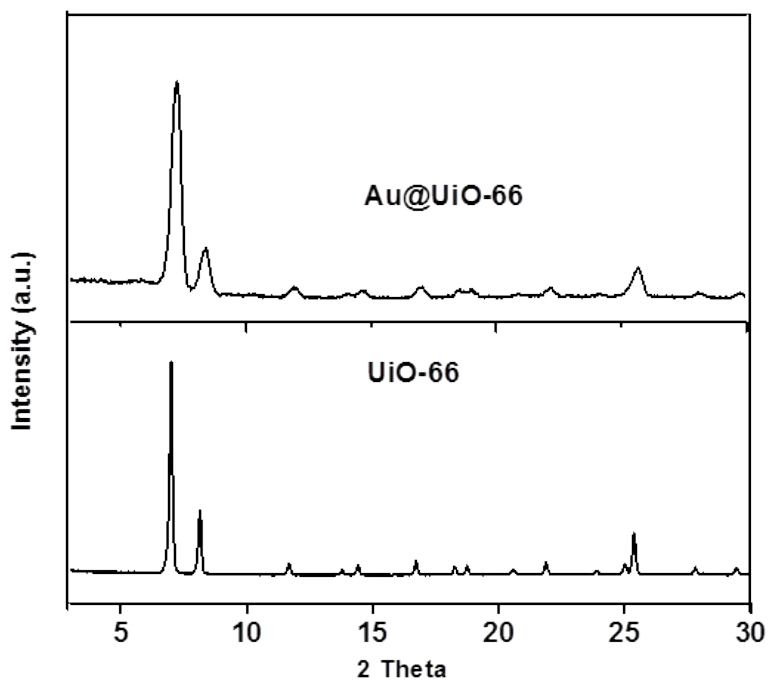


**Figure S20.** XRD diagrams of UiO-66 and Au/UiO-66.

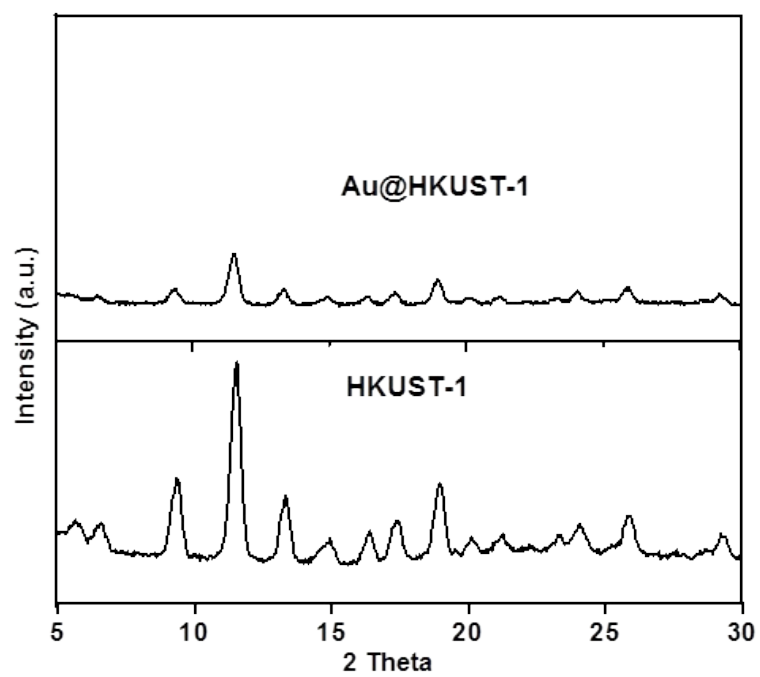


**Figure S21.** XRD diagrams of HKUST-1 and Au/HKUST-1.

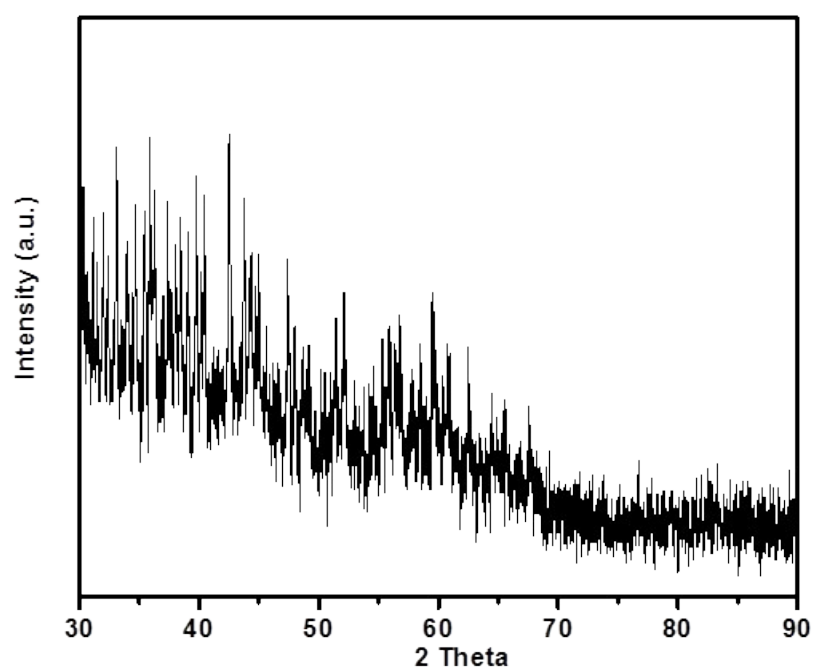


**Figure S22.** XRD diagrams of Au/MOF-808-SH in the 30-90° 2 theta region.

Note that in accordance with our microscopic observations (Section C-2 of the SI) and the previously reported study by Zhen-Da Lu *and co.*,<sup>14</sup> the absence of Au diffraction peaks in Au/MOF-808-SH could presumably correlated to the formation of ultra-small Au nanoparticles and low content.

### **C-5. UV-vis spectra of Au/MOF materials**

The UV-visible spectra of Au/MOFs materials show a LSPR band located at  $\lambda = 522$  nm;  $\lambda = 537$  nm;  $\lambda = 500$  nm;  $\lambda = 521$  nm and  $\lambda = 485$  nm, respectively for Au/MIL-101 (Cr), Au/MOF-808, Au/MOF-808-NH<sub>2</sub>, Au/UiO-66 and Au/HKUST-1 (Figure 2d, h, Figure S23). Due to the small size of the Au NPs in Au/MOF-808-SH and in Au/MIL-101 (Cr) -SH, no LSPR band is observed. Indeed, Kimura *et al.* reported that the appearance of a LSPR from Au NPs stabilized by sulfur ligands (mercaptosuccinic acid) depends on the size of the Au NPs.<sup>15</sup> They observed the appearance of a LSPR only when the Au diameter was  $\geq 1.94$  nm. Here, for Au/MOF-808-SH and Au/MIL-101 (Cr) -SH materials, the mean sizes of Au NPs ( $1.0 \pm 0.2$  nm and  $1.0 \pm 0.5$  nm respectively) are too small to support a LSPR.

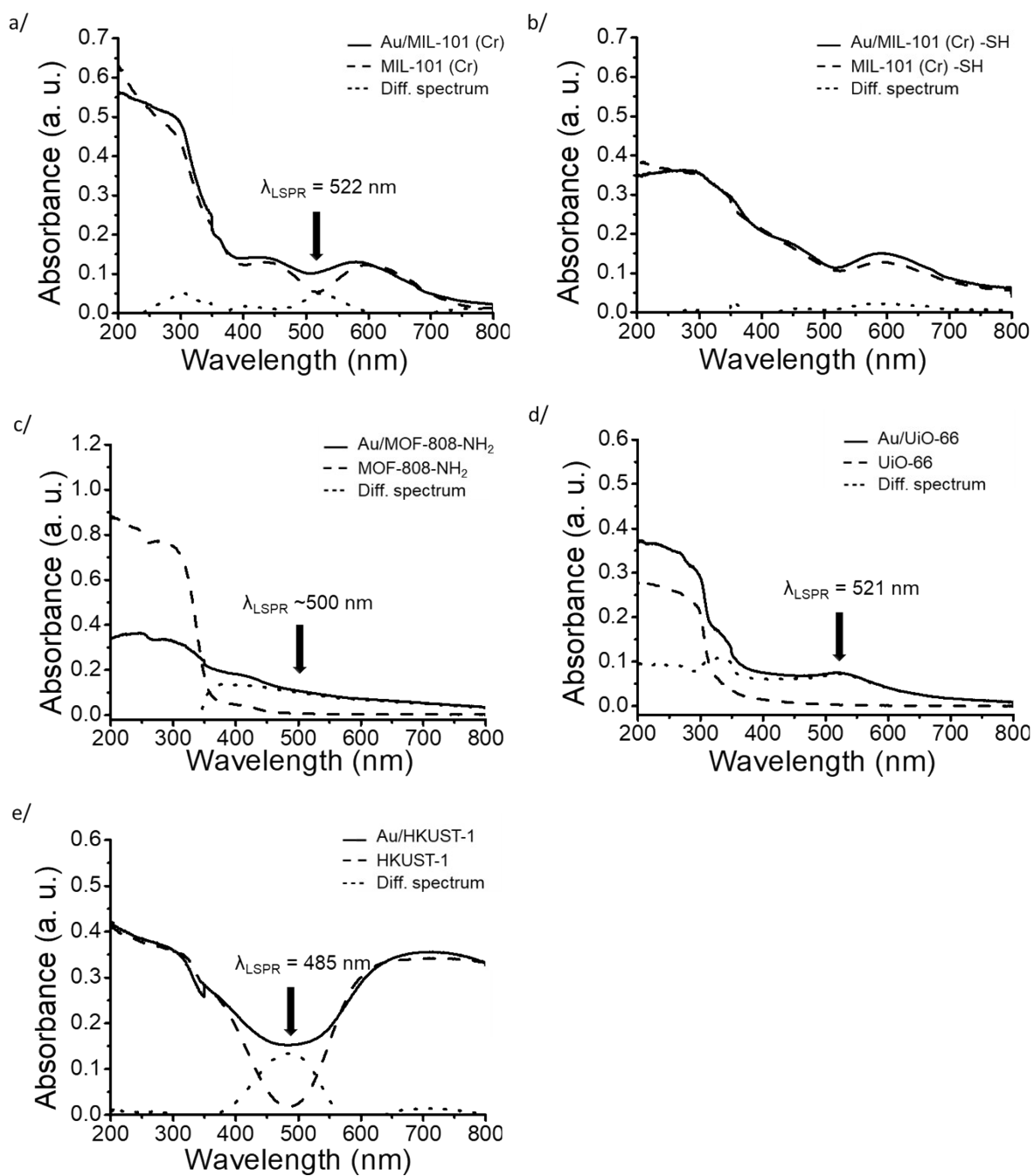


**Figure S23.** UV-vis spectra of Au/MOF (solid line) and MOF (dash line) materials for (a) MIL-101 (Cr); (b) MIL-101 (Cr) -SH; (c) MOF-808-NH<sub>2</sub>; (d) UiO-66; (e) HKUST-1. (In order to better view the LSPR band the differential spectra are added in dotted line).

## C-6. LEIS spectra of Au/MOFs and MOFs materials

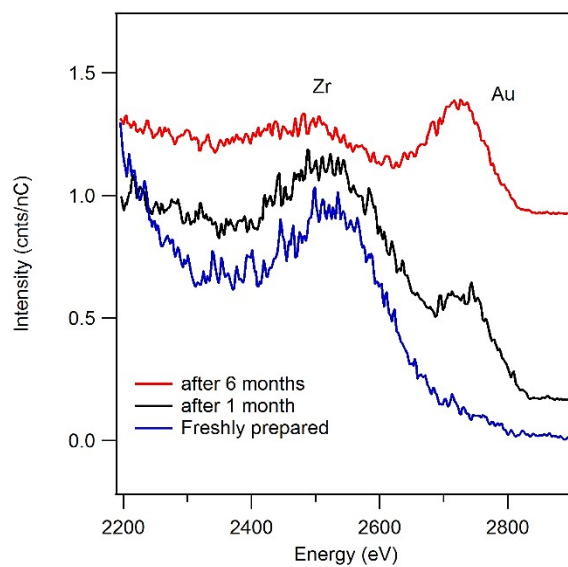


**Figure S24.** 3 keV He<sup>+</sup> LEIS spectra collected as a function of time after synthesis, showing migration of Au to the surface. Importantly, no sputtering has been performed, demonstrating that surface Au NPs can be readily detected.

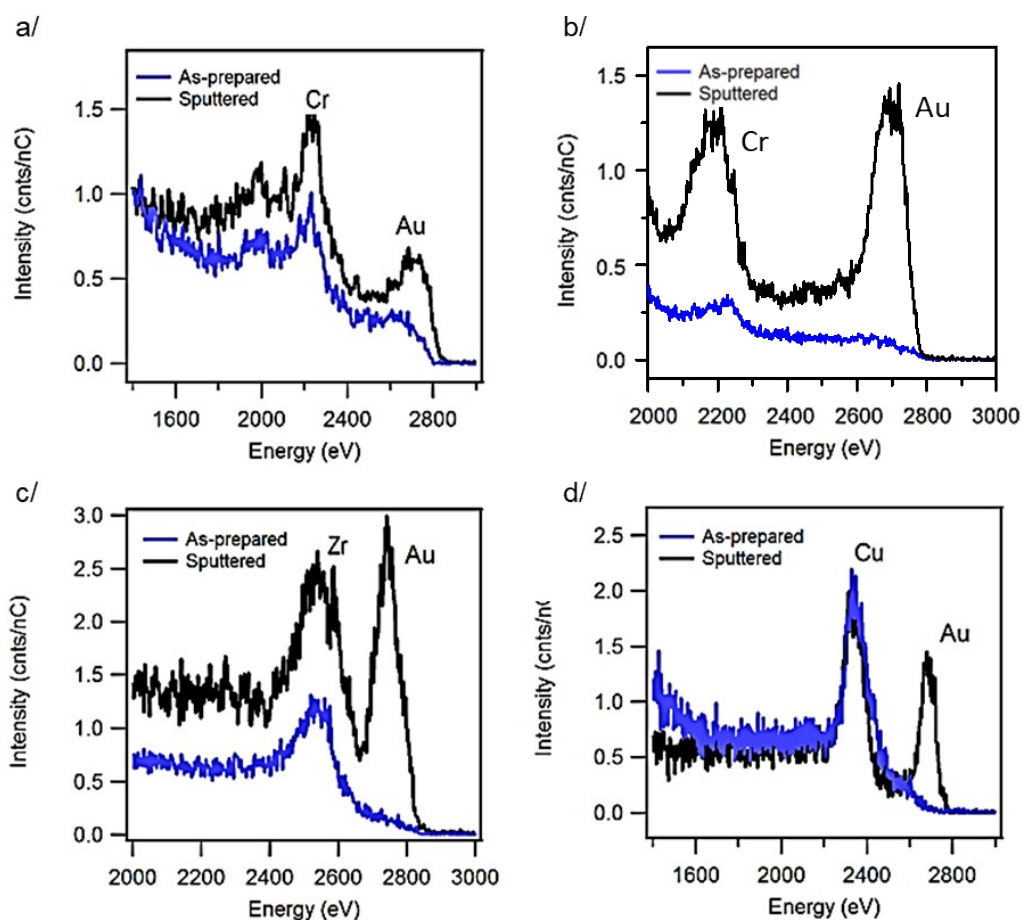


**Figure S25.** 3 keV He<sup>+</sup> LEIS spectra of (a) Au/MIL-101 (Cr); (b) Au/MIL-101 (Cr) -SH; (c) Au/UiO-66; and (d) Au/HKUST-1; before (blue) and after (black) a sputtering ( $4 \cdot 10^{14} \text{ cm}^{-2} \text{ Ar}^+$ ).

Note that the spectra of Au/MIL-101 (Cr) show a weak threshold feature within the Au binary collision region, although the apparent scattering threshold is observed at a lower energy than in the case of the spectra from the sputtered sample. Such a threshold in the background signal is indicative of subsurface Au, where the energy separation between the surface peak (e.g., in the sputtered spectrum) and the scattering threshold are determined by the thickness, composition, and density of the overlayer.<sup>16-19</sup> The fact that the background signal appears so much more prominent in the case of MOF MIL-101 (Cr) can be directly

correlated to the fact that, among all the MOFs studied here, MOF MIL-101 (Cr) has the largest pore size. A similar threshold in the background signal can be observed in the spectra of as-prepared Au/HKUST-1 (Figure S25d), but is less intense and shifted by a larger amount. This difference can be correlated to the relatively smaller pore size. In both cases, these data support the subsurface localization of Au within the MOF samples. Note that for MIL-101 (Cr) and MIL-101 (Cr) -SH, Cl can be observed (~2000 eV) and probably results from the gold salt (HAuCl<sub>4</sub>) used during the growth of Au NPs.

### **Supplemental Note 1: Charging of MOF samples during LEIS analysis**

Due to the insulating characteristics of the MOFs, considerable charging of the samples occurred even when neutralization was applied. Consequently, we observed variation in the positions of the peaks from one MOF to the next (e.g., variation of the position of the Au peak in Figure S25 or the Zr peak in Figure 3), before and after sputtering, and even in sequential measurements of the same MOF due to progressive charging. Importantly, however, the most important quantity for the analysis presented here for identification of surface elements is the separation between the peaks, which is independent of charging. In Figure S25 we manually corrected the energy axis to align the surface peaks of the metal atoms intrinsic to the MOF before and after sputtering simply to enable easy comparison, but note that this has no bearing on the relative separation between the peaks or the identification of Au in the spectra. We also note that discrepancies in the positions of the binary collision peaks from one MOF to the next (such as the Zr peak in Figure 3 and Figure S25 in three different MOFs) can also be influenced by inelastic processes,<sup>16</sup> which vary based on the details of the atomic and electronic structure of the material.

### C-7. *Ab initio* calculations performed on Au/MOF-808-SH

Calculations were performed in VASP<sup>20, 21</sup> at the density functional theory (DFT) level, using the vdW-DF exchange-correlation potential<sup>22-25</sup> to capture van der Waals interactions. The PAW potentials provided by VASP were implemented with an energy cutoff of 600 eV; only the  $\Gamma$  point was used. The MOF-808 unit cell consists of 270 atoms; three functional pmba groups (SH) were added to represent the functionalized MOF-808 (MOF-808-SH), creating a unit cell with 306 atoms. All binding energy and frequency calculations were performed on the fully relaxed (forces on all atoms were less than  $10^{-3}$  eV/Å) and periodic MOF-808-SH unit cell in the presence of gold in order to study nucleation, preferential binding locations, and identify experimental vibrational modes. Binding energies were calculated as energy differences between the bound systems and suitably defined individual fragments. Vibrational modes were calculated by a finite difference method—where atoms were typically displaced by 0.04 Å—and diagonalizing the resulting dynamical matrix under the constraints of applicable sum rules. Charge density rearrangements, which show the calculated gain and loss of charge upon introduction of a guest (in this case, the 16 atom Au cluster) are calculated by taking the 16Au-MOF-808(-SH) charge density and subtracting the individual charge densities of the isolated 16 atom Au cluster and MOF-808(-SH).

Figure S26 shows how the thiol groups sit in the pore of MOF-808-SH. Six SH groups occupy each “window” of the MOF-808, creating a barrier that Au clusters would have to diffuse through; note that there are four such windows in total per pore. The diameter of the opening in those windows created by the sulfur groups is approximately 5 Å wide (Figure S26b). The diameter of the 16 atom gold cluster measures 5.6 – 7.4 Å as the cluster is asymmetric; so physically, the 16 atom cluster would not be able to diffuse through the sulfur pore. However, even if the cluster was small enough to pass through the pore, the binding energy of a 16 atom cluster to one S group is calculated to be 1.68 eV (i.e.  $\sim 6 \times 1.68$  eV when

bound to 6 SH groups of one window or  $\sim 24 \times 1.68$  eV when bound to SH groups in all four windows), essentially indicating that the cluster “sticks” to the SH functionals. This energy is much too high to be overcome at room temperature and thus practically prevents any diffusion of the cluster through the MOF. The single atom binds even more strongly, effectively preventing diffusion. We have also tested the binding energy of the gold salt ( $\text{AuCl}_4$ ) and find that it does *not* bind to the sulfur of the SH functional and can thus easily diffuse. In summary, while the salt is free to diffuse because it is small enough to pass through the SH pore window and does not “stick” to the sulfur, the 16 atom gold cluster is too large and has too high of a barrier to overcome for diffusion to occur. Further, a single gold atom binds even more strongly and henceforth can also not diffuse.

To study how the  $-\text{SH}$  functional groups may aid in stabilizing the gold nanoparticles, we compare the binding energies of the 16 atom gold cluster to MOF-808 and MOF-808-SH. We find that the cluster binds to MOF-808 with a binding energy of 1.32 eV and to MOF-808-SH with 2.38 eV (Table S8), clearly showing that the  $-\text{SH}$  functional is providing additional stability due to the large gain in binding energy compared to the MOF without the functional, as the only difference between the models is the presence of the  $-\text{SH}$  functional. Furthermore, by analyzing the computed charge rearrangement caused by the 16 atom cluster binding to the SBU nodes of both MOF-808 and MOF-808-SH, we can identify how the  $-\text{SH}$  functional helps stabilize the 16 atom Au cluster. Figure S27 shows a clear, bond-like (strong charge gain between atoms) interaction between the 16 Au cluster and the OH of the SBU node for both the MOF-808 and MOF-808-SH. However, MOF-808-SH shows an additional bond-like interaction between the gold cluster and aromatic ring of the  $-\text{SH}$  functional whereas MOF-808 shows no additional charge gain interactions between the SBU node or the carboxylate linkers. In fact, no gain of charge (and little other charge rearrangement) is observed between the carboxylate groups and gold cluster for either system. This indicates that binding to the

MOF framework is mainly due to charge gain (bond type) interaction with the SBU node, but the presence of the –SH functional provides an additional bond-type interaction. The lack of interaction between the Au cluster and the carboxylate linker of MOF-808 is expected, as experimentally little to no shift in the carboxylate vibrational modes is observed (Figure 4d).

**Table S8. Binding Energy of Au.** The binding energy of a single gold atom and a 16-atom gold cluster is calculated at the ends of the SH functional group and near the SBU nodes where it interacts with the MOF framework. A positive number indicates favorable binding.

Cluster Size	MOF-808-SH		MOF-808
	Functional Group	SBU Node	SBU Node
Au <sub>1</sub>	2.32 eV	1.93 eV	
Au <sub>16</sub>	1.68 eV	2.38 eV	1.32 eV

**Table S9. Calculated Vibrational Modes.** Calculated frequencies for relevant vibrational modes. A mode in parentheses indicates the calculated frequency when gold is not present. The Au-O mode involves both the carboxylate oxygen of the organic linker of MOF-808 and the bridging oxygen of the SBU node.

Vibrational Mode	Calculated Frequency (cm <sup>-1</sup> )
Bridging O-H	3640 (3697)
Au-O	296
Au-S	254

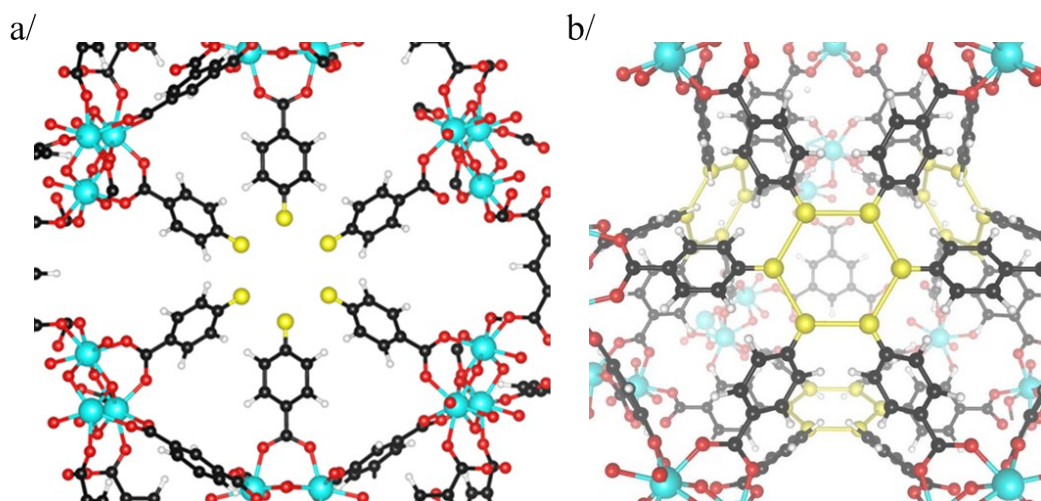


**Figure S26.** a) Six thiol groups occupying a “window” of MOF-808-SH. b) Four “windows” making up an inner pore that can accommodate Au NPs of up to 1.2 nm according to our computational model, encapsulated by the thiol groups. Here, the sulfur atoms are connected to form a hexagon for better visibility.

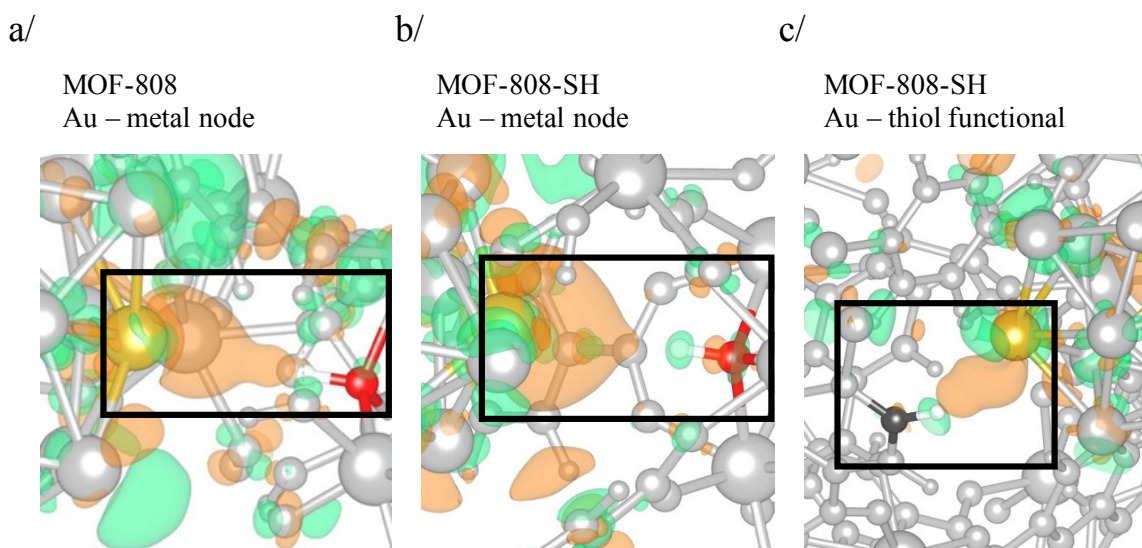


**Figure S27.** Charge rearrangement upon the addition of a 16 atom gold cluster at an isolevel of  $5 \times 10^{-4} e/\text{\AA}^{-3}$  where an orange isosurface indicates gain of charge and green a loss of charge. Non-interacting atoms are shown in grey while interacting atoms are colored as follows: Gold Au, red O, white H, and black C. The interaction with the MOF metal node is shown for (a) the MOF-808 and (b) MOF-808-SH. The cluster is closer to the metal node in MOF-808 and has a stronger bond-type interaction. The interaction of the 16 atom gold cluster with the thiol functional group to MOF-808-SH is shown in (c). The interaction region is also boxed to further guide the eye.

## C-8. IR and Raman spectroscopic study of Au/MOFs and MOFs materials

### C-8.1. Evidence of Au-O stretch mode

Spectroscopic methods such as IR absorption and Raman scattering are most effective to identify the formation of chemical bonds. We have therefore performed extensive measurements during the nucleation and growth of Au NPs both before and after UV-vis irradiation. We find that the IR spectra of MOF-808 and MOF-808-SH are not affected by UV-vis irradiation in an ethanolic environment (Figure S28), pointing to their stability.

In order to confirm that the mode observed in the Raman spectra at 262 and 259  $\text{cm}^{-1}$  can be assigned to the Au-O stretch for MOF-808 and MOF-808-SH, respectively, a Raman spectrum of the gold  $\text{HAuCl}_4$  precursor alone was recorded (Figure S29): there are no vibrational modes in the 300-400  $\text{cm}^{-1}$  Raman shift region, ruling out the potential contribution of the Au-Cl mode. This observation confirms that  $\text{HAuCl}_4$  is indeed decomposed and that the mode observed at  $\sim 260 \text{ cm}^{-1}$  in Au/MOFs is associated specifically with reduced Au, hence can be assigned to the Au-O bond.

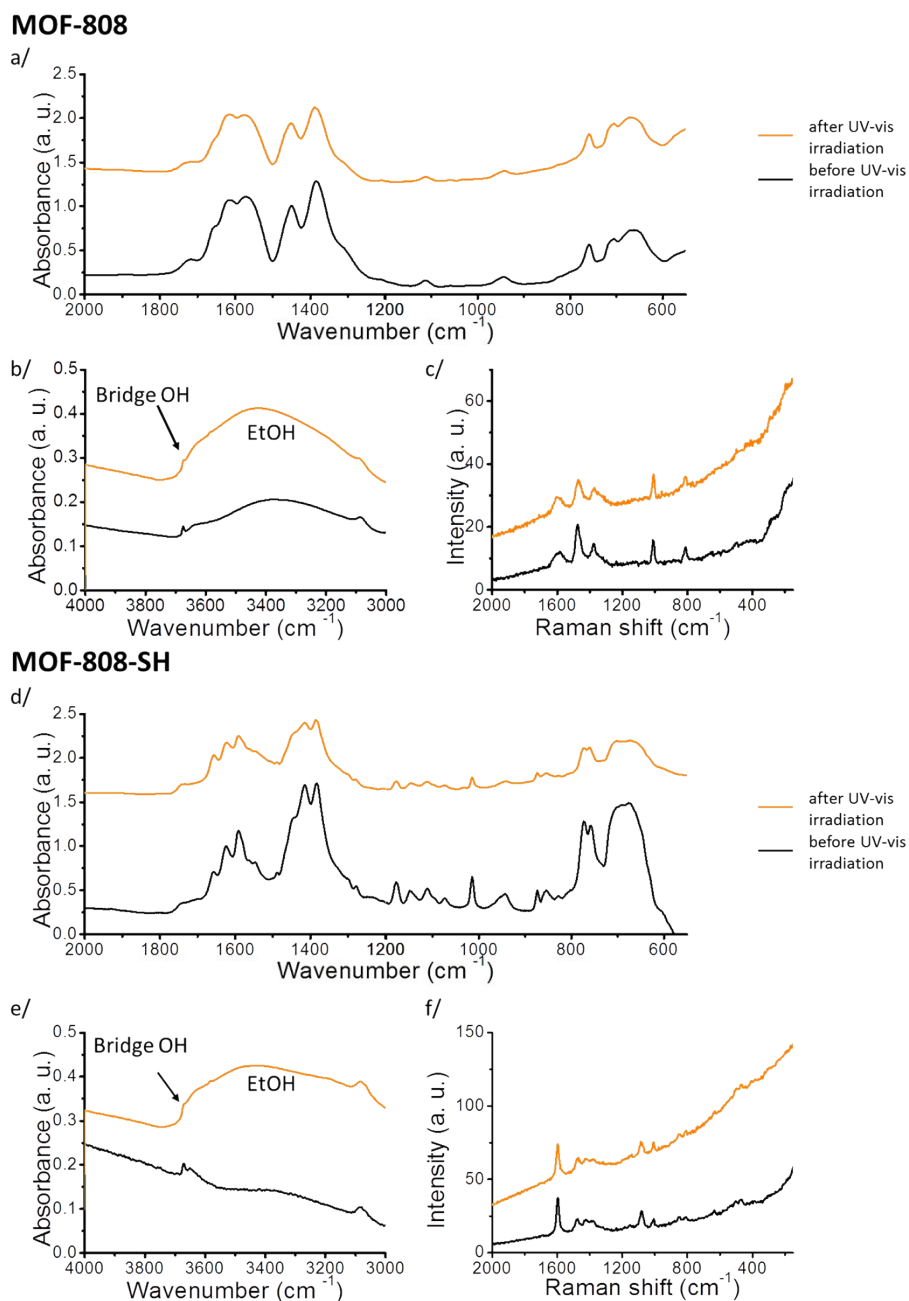


**Figure S28.** Infrared spectra: (a) 2000-550  $\text{cm}^{-1}$  region; and (b) 4000-3000  $\text{cm}^{-1}$  region; (c) Raman spectra of MOF-808 (A); and MOF-808-SH (B) before (black) and after (orange) UV-vis irradiation (alone) in ethanolic solution during 1 h 30.

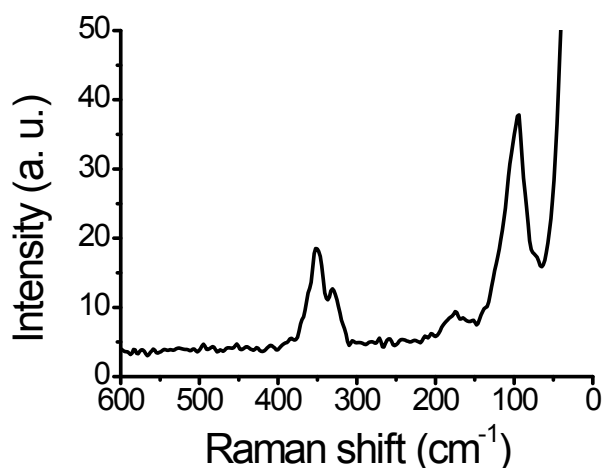


**Figure S29.** Raman spectrum of H[AuCl<sub>4</sub>].

In the Au/MOF-808-SH sample, there are two stretching modes that should be observable within the same frequency range:  $\nu(\text{Au-O})$  and  $\nu(\text{Au-S})$ . Therefore, we postulate that they may be too close to separate, both around 260 cm<sup>-1</sup> in Figure 5b. We tested that this mode is definitely associated with gold by recording a spectrum obtained on a sample in which 10 times less H[AuCl<sub>4</sub>] precursor was used (Figure S30) and noting that at best only a very weak feature can be seen at ~260 cm<sup>-1</sup>, expected for Au-S bonds above the pore windows, which are expected to be formed initially, i.e. before Au-O bonds are established.

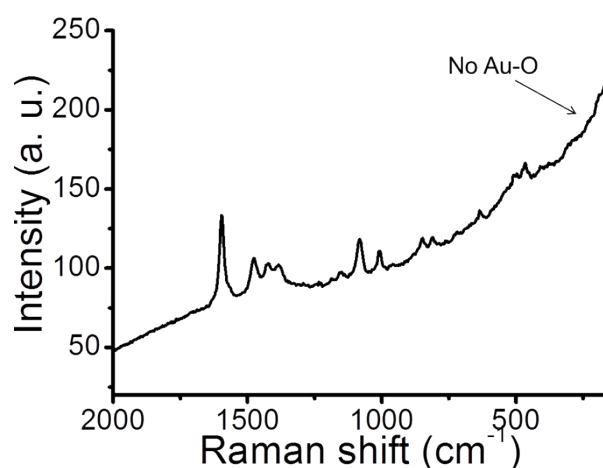


**Figure S30.** Raman spectrum of Au/MOF-808-SH synthesized with 10 times less of HAuCl<sub>4</sub> precursor by the photo-reduction method.

In conclusion, there is a reaction between the Au NPs and the hydroxyl groups, resulting in the loss of H and the formation of a Au-O bond in the MOF-808 and MOF-808-SH.

#### **Interaction of Au with ligands in other potential MOFs:**

We now explore the interaction of Au in other MOFs considered for confining Au NPs by focusing on both the OH groups and the Au-O modes.

*For UiO-66*, the OH stretch intensity weakens but does not completely disappear. This indicates that not all the -OH bridge groups react due to the weak pore size of UiO-66 (Table 1): the reduced volume of the pores introduces steric hindrance that prevent complete access of the Au NPs to the nodes. The Raman spectrum of Au/UiO-66 does however exhibit a reasonably strong Au-O stretch mode located at 253 cm<sup>-1</sup>. Keeping in mind that the Raman intensity is controlled by factors other than concentration (e.g. enhancement), these observations suggest that there is an interaction between the Au NPs and the bridge -O (Figure S32d, Figure S33d).

For *Au/MOF-808-NH<sub>2</sub>*, the absorption of the stretch modes associated with the primary amine groups, initially located at 3228 cm<sup>-1</sup> and 3389 cm<sup>-1</sup>, disappears all together, suggesting that there is a reaction between the Au NPs and the -NH<sub>2</sub> groups of MOF-808-NH<sub>2</sub> (Figure S32b). Note that the Raman Au-N stretch cannot be detected due to a strong fluorescence background that substantially degrades the sensitivity (Figure S33b).

For both *MIL-101 (Cr)* and *HKUST-1*, which do not have bridge -OH groups at their node,<sup>3, 7, 8</sup> the detected OH stretch absorption (originating only from H<sub>2</sub>O) is conserved after the Au NPs growth (Figure S32a, d). We therefore conclude that, due to the nature of the -OH<sub>2</sub> nodes groups and independent from the pores sizes that are most different for Au/MIL-101 (Cr) and Au/HKUST-1 materials (Table 1), there is no interaction of Au between the Au NPs and the nodes. However, there is a clear vibrational mode assigned to Au-O stretch mode in the Raman spectra at 267 cm<sup>-1</sup> for Au/MIL-101 (Cr) (Figure S33a, c), suggesting that Au is reacting with the bdc linkers instead of the -OH<sub>2</sub> groups characterized by the mode at 3735 cm<sup>-1</sup> (Figure S32a).

In conclusion, the Au NPs are found to react, totally or partially, with OH groups in MOFs that have bridge OH at their node, or with the oxygen of the ligands for those that do not have bridge OH. Note that for MOFs with OH groups, we cannot exclude that Au also reacts with oxygen of the ligands. This point is addressed next in section C-8-2.

### *C-8.2. Evidence of interaction between the carboxylate groups and Au NPs*

Based on our previous study of six different MOFs, we have assigned 6 main peaks in the IR spectrum to modes associated with carboxylate groups. For MOF-808-SH, they are the  $\nu_{\text{sym}}(\text{COO-Zr})$  at 1658 cm<sup>-1</sup>, 1624 cm<sup>-1</sup> and 1591 cm<sup>-1</sup> and  $\nu_{\text{asym}}(\text{COO-Zr})$  at 1446 cm<sup>-1</sup>, 1415 cm<sup>-1</sup> and 1384 cm<sup>-1</sup> (Figure 5d).<sup>26</sup> The relative intensities of these vibrational modes are modified after the synthesis of Au NPs. In the differential IR spectrum resulting from the

subtraction between the Au/MOF-808-SH and MOF-808-SH spectra, a similar profile of 2 x 3 new modes appears at shifted frequencies: 1650 cm<sup>-1</sup>, 1632 cm<sup>-1</sup>, and 1612 cm<sup>-1</sup> and 1568 cm<sup>-1</sup>, 1525 cm<sup>-1</sup> and 1482 cm<sup>-1</sup> (Figure 5d). Respectively, the three first and the three last frequency modes are assigned to  $\nu_{\text{sym}}(\text{COO}^- \text{-Au})$  and to  $\nu_{\text{asym}}(\text{COO}^- \text{-Au})$  of carboxylate groups weakly interacting with Au NPs. Indeed, weak interactions induce frequency shifts towards the higher wavenumbers. Despite the perturbation these modes, pointing to a weak interaction between the Au NPs and the carboxylate groups of the linkers and/or the functional groups (Figure 5c), the major part of the carboxylate groups are always bound on the SBU nodes. Indeed, in the Au/MOF-808-SH spectrum, the major vibrational modes at 1653 cm<sup>-1</sup>, 1623 cm<sup>-1</sup> and 1590 cm<sup>-1</sup> ( $\nu_{\text{sym}}(\text{COO}^- \text{-Zr})$ ) and 1451 cm<sup>-1</sup>, 1414 cm<sup>-1</sup> and 1387 cm<sup>-1</sup> ( $\nu_{\text{asym}}(\text{COO}^- \text{-Zr})$ ) remain at the same frequencies as in MOF-808-SH: at 1658 cm<sup>-1</sup>, 1624 cm<sup>-1</sup>, 1591 cm<sup>-1</sup>, ( $\nu_{\text{sym}}(\text{COO}^- \text{-Zr})$ ), and 1446 cm<sup>-1</sup>, 1415 cm<sup>-1</sup> and 1384 cm<sup>-1</sup> ( $\nu_{\text{asym}}(\text{COO}^- \text{-Zr})$ ) (Figure 5d).

In conclusion, this weak interaction of gold with the carboxylate groups (linkers btc and/or functional groups pmba) connected on the SBU nodes supports a localization of the Au NPs inside the pores of the host MOF-808-SH with sections of the NP outer surface in the vicinity of the ligand. This assessment is in agreement with the *ab initio* calculations performed on Au/MOF-808-SH (section C-7, SI).

No clear modifications are observed in the 2000-550 cm<sup>-1</sup> IR frequency spectral region for Au/MOF-808 compared to MOF-808 materials (Figure 4d). The differential spectrum does not show new modes for Au/MOF-808 contrary to Au/MOF-808-SH materials. For Au/MOF-808, the nanoparticles interact only with the bridge -O of the nodes and not with the carboxylate groups of the linker btc.

A blue shift of the carboxylate stretch modes is observed in the Au/MOFs materials IR spectra: Au/MIL-101 (Cr) at  $\nu_{\text{sym}}(\text{COO}) = 1620 \text{ cm}^{-1}$  and  $\nu_{\text{asym}}(\text{COO}) = 1400 \text{ cm}^{-1}$ ; Au/MOF-

808-NH<sub>2</sub> at  $\nu_{\text{sym}}(\text{COO}) = 1622 \text{ cm}^{-1}$  and  $\nu_{\text{asym}}(\text{COO}^-) = 1387 \text{ cm}^{-1}$ ; and Au/HKUST-1 at  $\nu_{\text{sym}}(\text{COO}) = 1651 \text{ cm}^{-1}$  and  $\nu_{\text{asym}}(\text{COO}) = 1375 \text{ cm}^{-1}$  (Figure S32a, b, d). This shift may be associated with some interaction of varying strength between carboxylates groups and gold. Indeed, for example in Au/Mil-101 (Cr), a very strong mode is observed in the Raman spectra at  $267 \text{ cm}^{-1}$  (Figure S33a). This mode, assigned to a stretch of the Au-O bonds, must involve the formation of bonds between the gold and oxygen atoms of the carboxylate groups since no interaction was observed in this system with the -OH<sub>2</sub> groups of the nodes (Figure S32a). For Au/UiO-66, no strong effects are observed in the carboxylate groups modes, which confirms very weak interactions on average between the Au NPs and the nodes of the MOFs due a too strong confinement by the pore structures.

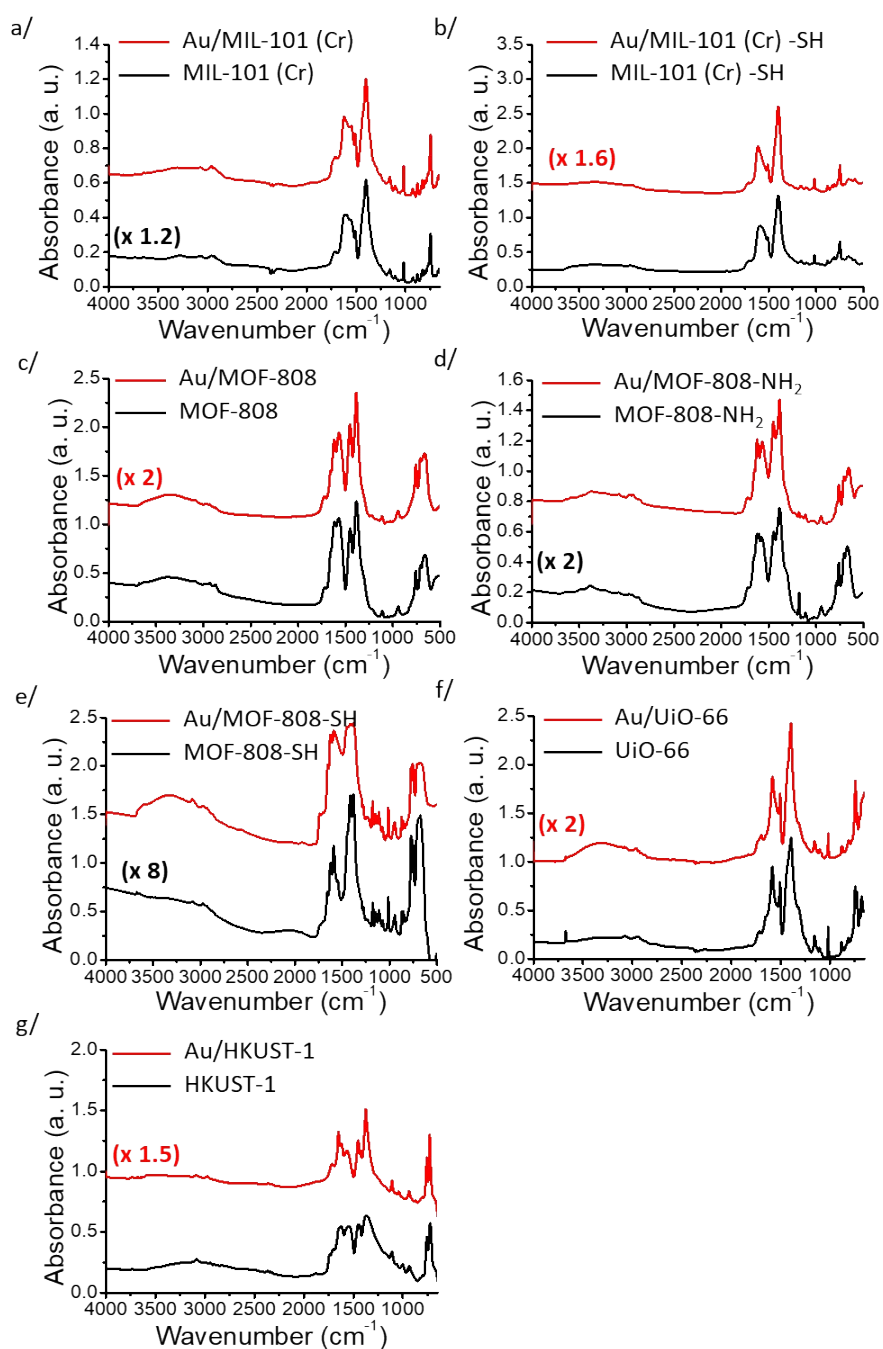


**Figure S31.** General Infrared spectra of Au/MOFs (red curves) and MOFs (black curves) for: (a) MIL-101 (Cr); (b) MIL-101 (Cr) -SH; (c) MOF-808; (d) MOF-808-NH<sub>2</sub>; (e) MOF-808-SH; (f) UiO-66 and (g) HKUST-1.

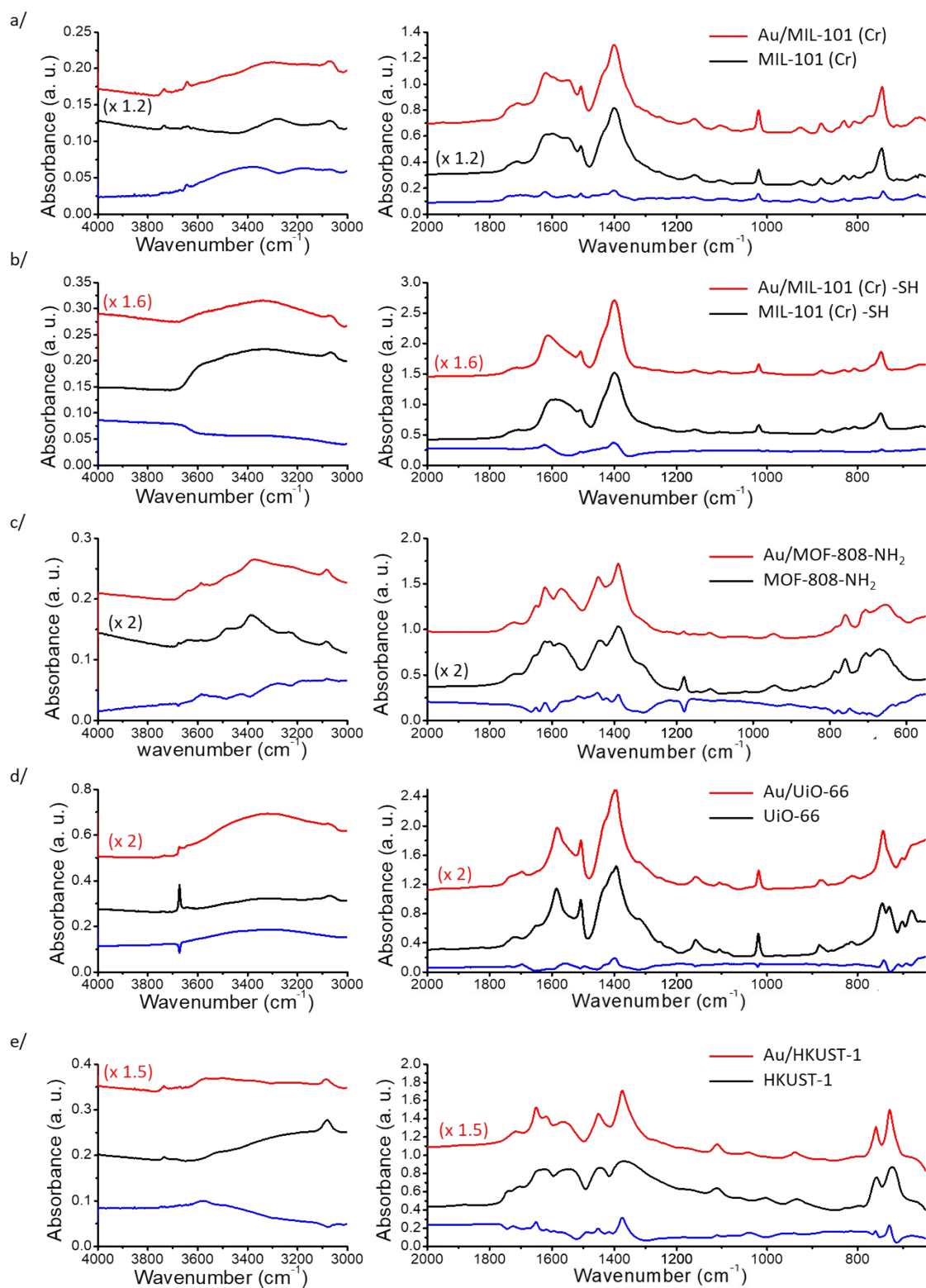


**Figure S32.** Infrared spectra of Au/MOFs (red curves) and MOFs (black curves) for: (a) MIL-101 (Cr); (b) MIL-101 (Cr) -SH; (c) MOF-808-NH<sub>2</sub>; (d) UiO-66 and (e) HKUST-1. Differential spectra are depicted as blue.

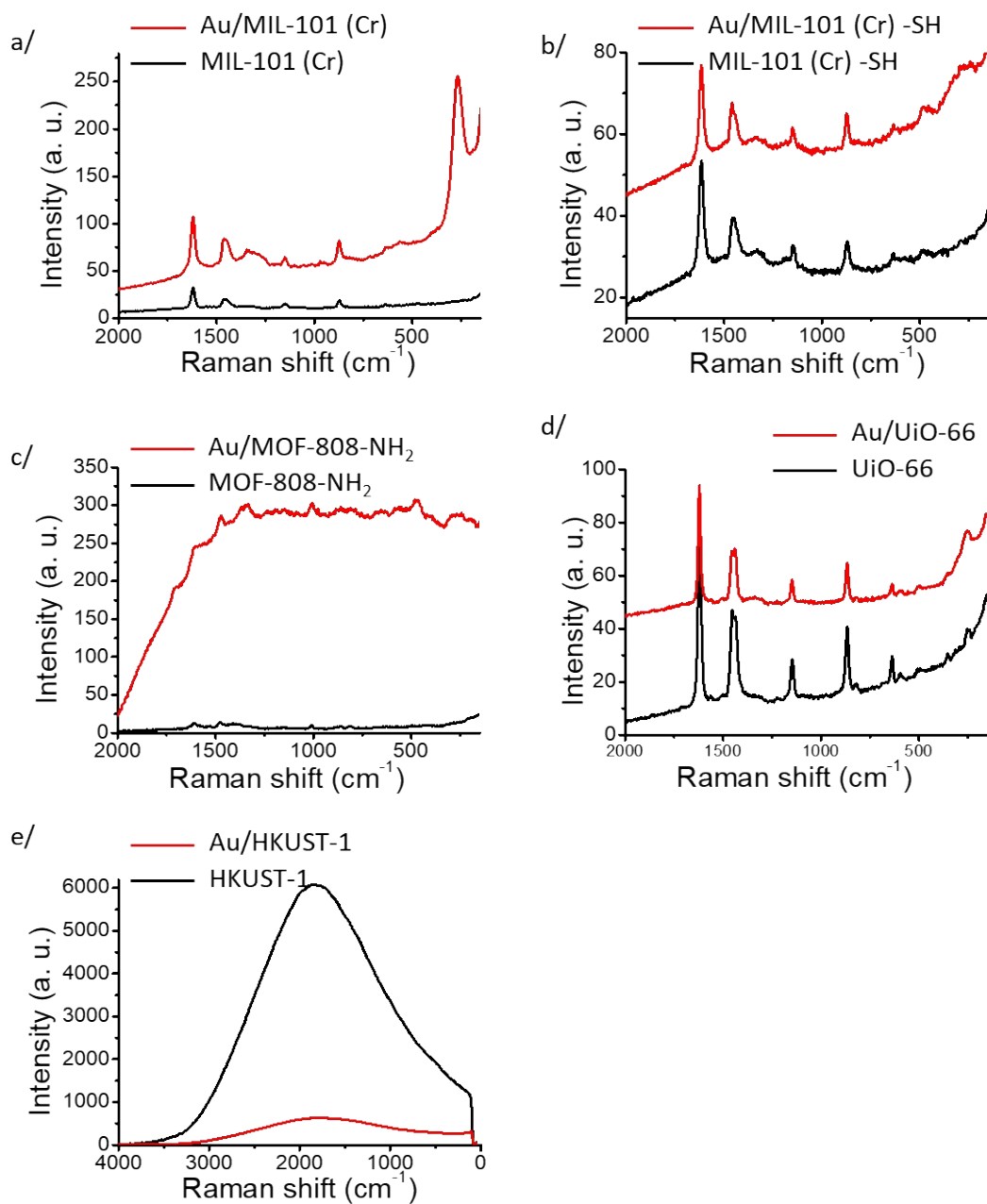


**Figure S33.** Raman spectra of Au/MOFs (red curves) and MOFs (black curves) for: (a) MIL-101 (Cr); (b) MIL-101 (Cr) -SH; (c) MOF-808-NH<sub>2</sub>; (d) UiO-66 and (e) HKUST-1.

### C-9. Influence of the functionalization by -SH groups on the strong stabilization of Au NPs in MIL-101 (Cr) -SH

Despite the size of its pores (larger than those of MOF-808-SH, see Table 1), MIL-101 (Cr) -SH is able to stabilize small Au NPs (average size:  $1.0 \pm 0.2$  nm) in contrast to unfunctionalized MIL-101 (Cr) (Au NPs average size:  $4.8 \pm 2.3$  nm, much larger than the pore size). In fact, the size of Au NPs in MIL-101 (Cr) -SH is similar to that of Au NPs in Au/MOF-808-SH (Au NPs average size:  $1.0 \pm 0.5$  nm) (Figure 2f, Figure S4). The size extracted from HRTEM observations is consistent with the absence of any LSPR band in the UV-vis spectrum of Au/MIL-101 (Cr) -SH, which indicates that the Au NPs have a size less than 2 nm (Figure S23).<sup>15</sup> The LEIS spectrum confirms that Au NPs are localized within the MOF crystals (Figure S25b). Compared to MIL-101 (Cr) -SH, the IR spectrum of Au/MIL-101 (Cr) -SH exhibits a blue shift of the carboxylate stretch modes:  $\nu_{\text{sym}}(\text{COO}) = 1612 \text{ cm}^{-1}$  and  $\nu_{\text{asym}}(\text{COO}) = 1400 \text{ cm}^{-1}$  (Figure S32b), which results from interaction between carboxylate and gold as described for the other MOFs in Section C-8.2. However, this blue shift is less important in Au/MIL-101 (Cr) -SH (+  $7 \text{ cm}^{-1}$ ) than in Au/MIL-101 (Cr) (+  $10 \text{ cm}^{-1}$ ) (Figure S32a, b) and the Au-O mode in the Raman spectrum is also less intense in Au/MIL-101 (Cr) -SH (at  $260 \text{ cm}^{-1}$ ) than in Au/MIL-101 (Cr) (at  $267 \text{ cm}^{-1}$ ), although it is the strongest signal assigned to Au-O mode among all the MOFs measured (Figure S33a, b). As for the Au/MOF-808-SH system, these results suggest that the main interactions are stronger between the SH functional groups and gold than with the oxygen atoms of the SBU node. The conclusion is that the SH functional groups ensure a strong stabilization of the Au NPs within the center of the pores (between the four S hexagonal windows).

## C-10. Characterization of Ti transmuted Zr-based MOFs materials

Here, we used transmetalation to dope MOF-808-SH with titanium since the recent discovery of an enhanced photocatalytic activity for Ti-based MOFs was demonstrated for the hydrogen evolution reaction (HER) and photocatalytic CO<sub>2</sub> reduction.<sup>27, 28</sup> A new post-synthetic route, inspired by *Cohen et al.* with TiCl<sub>4</sub>(THF)<sub>2</sub>, is developed here with the TiCl<sub>4</sub> precursor (0.67 mol/Zr at.) at room temperature in a toluene suspension of MOF-808-SH (Section A-2.7, SI) to replace a part of the zirconium atoms of the SBU nodes by titanium atoms in MOF-808-SH(Ti) (Figure S34a).<sup>6</sup> In this case, the post-synthetic exchange developed here is performed at room temperature for a relatively short time (30 min) and with a different precursor from the one used by *Cohen et al.*<sup>6</sup> Furthermore, the sample is rinsed with anhydrous toluene after the transmetalation reaction in order to avoid the reaction between the residual TiCl<sub>4</sub> precursor and air, which can produce TiO<sub>2</sub> nanoparticles or TiO<sub>2</sub> coatings onto MOFs. A recent publication of *Cohen et al.* highlights the formation of titanium oxide coatings onto MOFs by using TiBr<sub>4</sub>, TiCp<sub>2</sub>Cl<sub>2</sub> or TiCl<sub>4</sub>(THF)<sub>2</sub> precursors and reveals that such surface coating can be avoided by applying a different procedure (several days at 80 °C in demethylformamide).<sup>29</sup> Here, we use microscopy (Figure S36) to establish that the post-synthetic route used with TiCl<sub>4</sub> leads to the transmetalation reaction as no nanoparticles and no titanium oxide coating onto MOFs crystals are observed. Moreover, the covalent bonding between Ti and carboxylate groups of the linkers btc is clearly observed by IR spectroscopy (Figure S34), which confirms the transmetalation reaction inside the MOF. Furthermore, Ti element is evidenced by XPS (Figure S39). Photo-reduction of Ti-doped MOF produces Au/MOF-808-SH(Ti) following the same procedure previously described (Figure S34a), as confirmed next.

There are distinct and strong modes in the IR spectra after transmetalation at 1658 cm<sup>-1</sup> in MOF-808-SH(Ti) and 1656 cm<sup>-1</sup> in Au/MOF-808-SH(Ti) (Figure S34b). For a better

understanding, the differential spectrum of MOF-808-SH(Ti) compared to MOF-808-SH is presented (Figure S34b, grey curve) and reveals the asymmetric and symmetric carboxylate stretching vibrations respectively at  $1659\text{ cm}^{-1}/1571\text{ cm}^{-1}$  and  $1398\text{ cm}^{-1}/1361\text{ cm}^{-1}$  assigned to the COO-Ti bonds vibrational mode.<sup>30-32</sup> Importantly, the presence of the OH stretching mode at  $3668\text{ cm}^{-1}$  (Figure S34b) is not affected by the introduction of titanium atoms, confirming that the bridge -OH of the SBU nodes do not react with the  $\text{TiCl}_4$  precursor. Moreover, the HRTEM observations (Figure S36) of MOF-808-SH(Ti) do not show the presence of titanium oxide nanoparticles. Energy dispersive x-ray spectrometry (EDS) analysis is further used to quantify the relative concentration of Zr/Ti at the SBUs: 18% of the SBU nodes Zr atoms are replaced by Ti atoms (Figure S37a). This combined characterization demonstrates that titanium atoms are chemically bound with the carboxylates groups of the btc linkers and pmba functional groups (Figure S34a) without the formation of titanium oxide nanoparticles as by-products of the transmetalation, i.e. they replace Zr atoms.

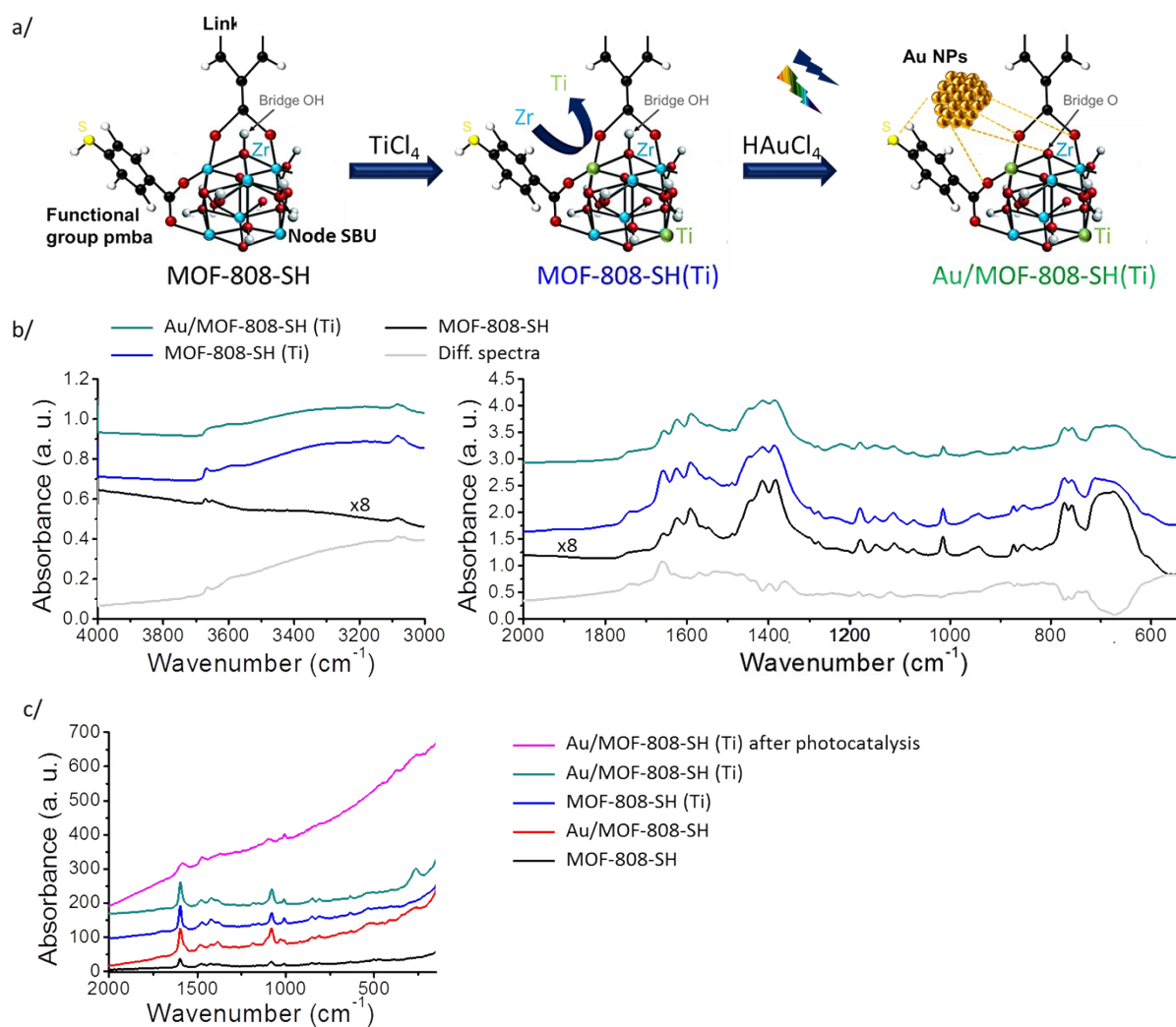


**Figure S34.** (a) Scheme of the post-synthetic transmetalation and photo-reduction routes, respectively to dope MOF-808-SH with Ti and grow Au NPs inside the MOF structure; (b) infrared and (c) Raman spectra of MOF-808-SH (black), Au/MOF-808-SH (red), MOF-808-SH(Ti) (blue), Au/MOF-808-SH(Ti) before (blue-green) and after photocatalysis (violet). The infrared differential spectrum between MOF-808-SH(Ti) and MOF-808-SH is depicted in grey.

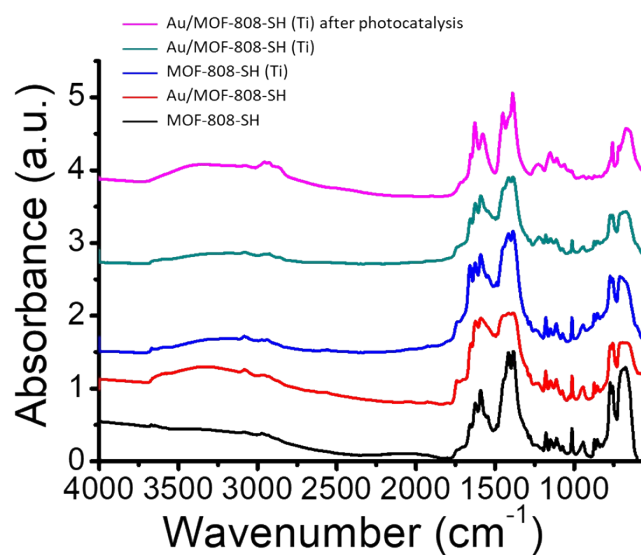


**Figure S35.** Global IR spectra of MOF-808-SH (black), Au/MOF-808-SH (red), MOF-808-SH(Ti) (blue), and Au/MOF-808-SH(Ti) before (green) and after photocatalysis (violet).

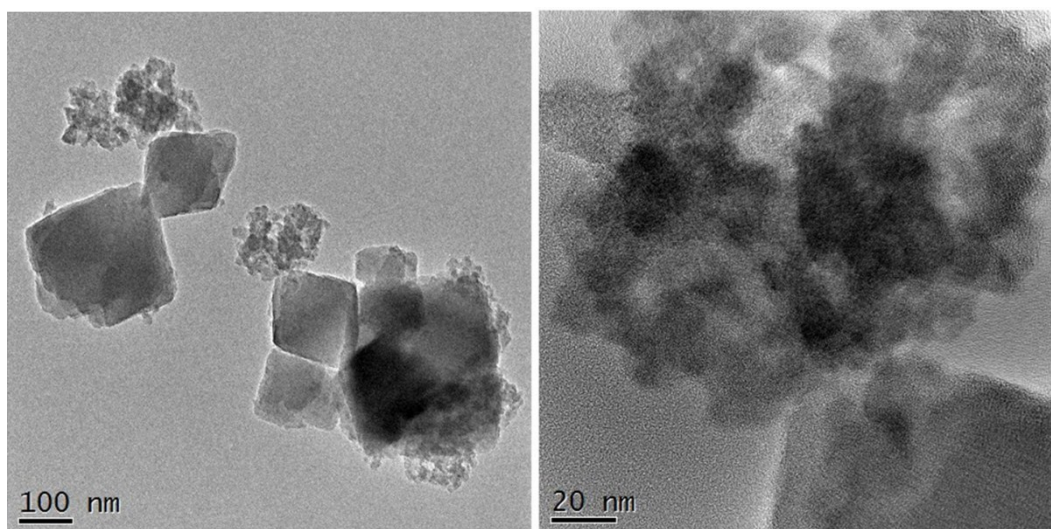


**Figure S36.** HRTEM observations of the MOF-808-SH(Ti) material. Only the MOF crystals are observed, no TiO<sub>x</sub> nanoparticles and no TiO<sub>x</sub> coatings onto MOF crystals are visible.

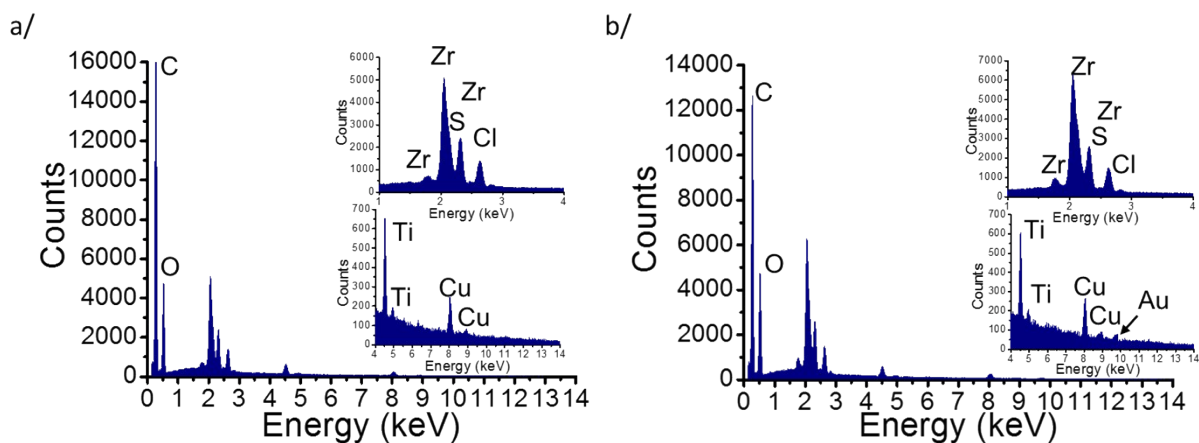


**Figure S37.** EDS spectra of MOF-808-SH(Ti) (a) before and (b) after Au NPs growth.

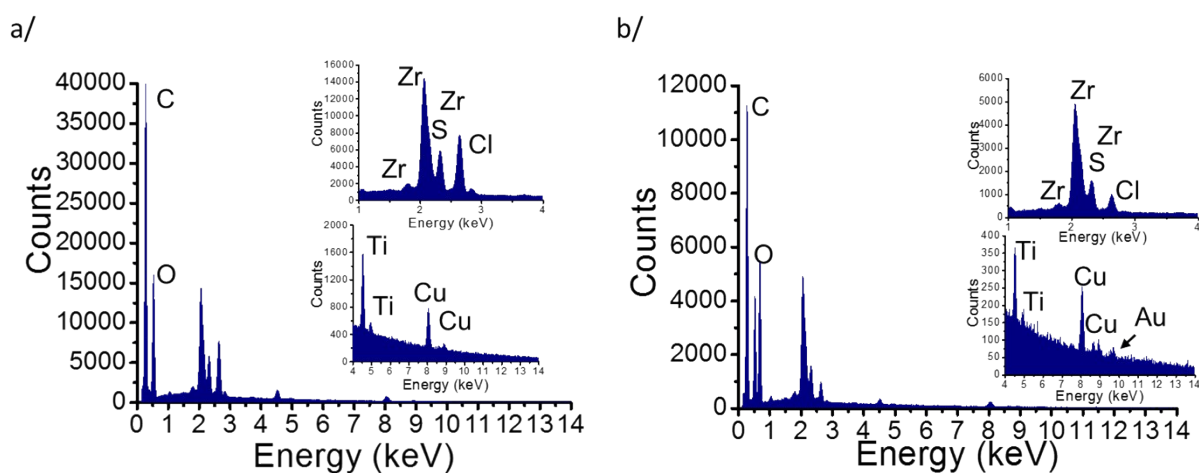


**Figure S38.** EDS spectra of Au/MOF-808-SH(Ti) (a) before and (b) after photocatalysis.

**Table S10.** Atomic and mass percentage for C, O, Zr, S, Cl, Ti, Cu, Au elements for MOF-808-SH(Ti) and Au/MOF-808-SH(Ti) materials. Note that the copper element results from the copper tape used during the measurements.

Element	MOF-808-SH(Ti)				Au/MOF-808-SH(Ti)			
	before Au NPs growth		after Au NPs growth		before photocal.		after photocal.	
	at%	Wt%	at%	Wt%	at%	Wt%	at%	Wt%
C	77.46	63.45	75.68	61.83	73.90	56.75	73.12	56.23
O	18.62	20.32	20.22	22.00	20.89	21.37	22.17	22.71
Zr	1.56	9.72	1.46	9.03	2.20	12.81	2.22	12.94
S	1.04	2.28	0.83	1.82	1.35	2.76	1.03	2.11
Cl	0.57	1.38	1.16	2.80	0.72	1.63	0.56	1.28
Ti	0.35	1.15	0.27	0.88	0.35	1.06	0.21	0.64
Cu	0.39	1.70	0.38	1.64	0.45	1.84	0.55	2.23
Au	0.00	0.00	0.00	0.00	0.14	1.77	0.15	1.87

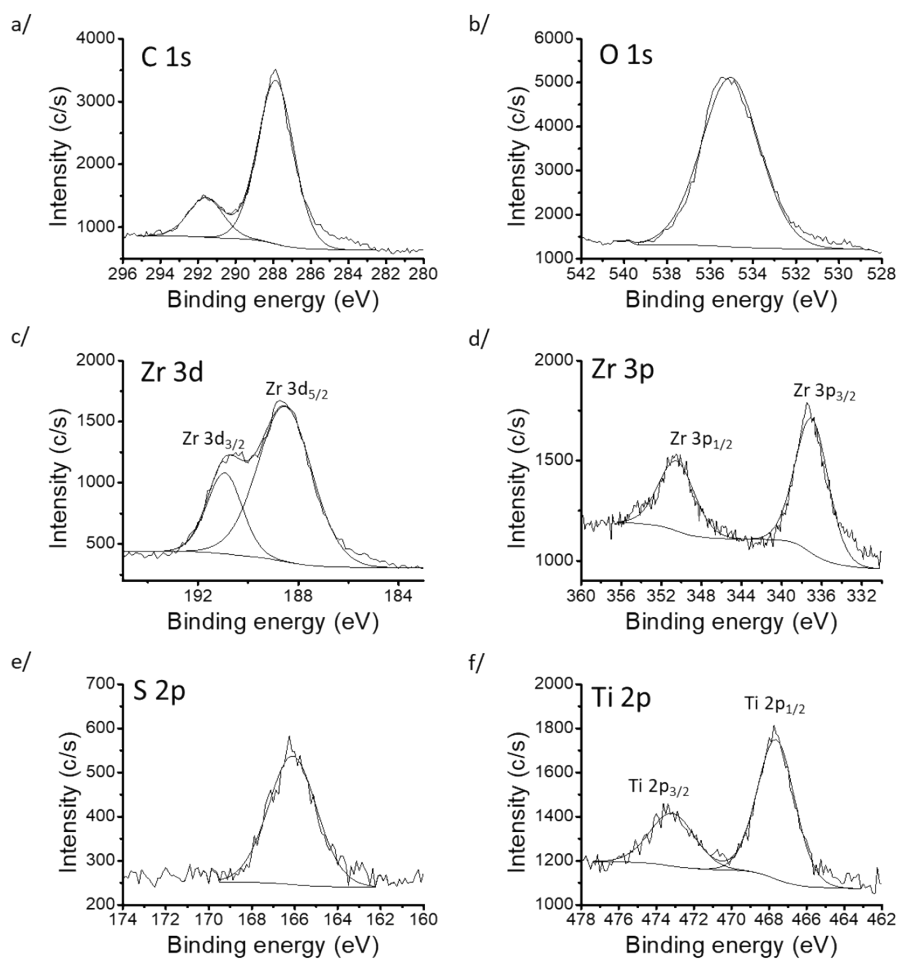


**Figure S39.** XPS spectra of Ti-doped MOF-808-SH (Ti): (a) C 1s, (b) O 1s, (c) Zr 3d<sub>3/2,5/2</sub>, (d) Zr 3p<sub>1/2,3/2</sub>, (e) S 2p; (f) Ti 2p<sub>1/2, 3/2</sub> regions.

**Table S11.** Main components positions ( $\pm 0.1$  eV), FWHM ( $\pm 0.05$  eV) for each element (C, O, Zr, Ti) for MOF-808-SH (Ti) material:

	C 1s		O 1s	Zr 3p		Zr 3d		S 2p	Ti 2p	
				Zr 3p <sub>1/2</sub>	Zr 3p <sub>3/2</sub>	Zr 3d <sub>3/2</sub>	Zr 3d <sub>5/2</sub>		Ti 2p <sub>1/2</sub>	Ti 2p <sub>3/2</sub>
MOF-808-SH (Ti)	290.6	286.8	534.0	349.4	336.0	189.9	187.5	165.1	472.1	466.6
	(2.2)	(2.3)	(3.2)	(4.2)	(3.9)	(1.7)	(2.5)	(2.8)	(2.8)	(2.4)

### C-11. Rate measurement of hydrogen production

Surprisingly, an activation period of 48 h is observed in Figure 6e for Au/MOF-808-SH(Ti). Indeed, the hydrogen production mean rates evolve respectively from 0.15, 0.04, 0.20 and 0.12  $\mu\text{mol H}_2\cdot\text{g}^{-1}\cdot\text{h}^{-1}$  before 48h, to 0.13, 0.03, 0.42 and 1.50  $\mu\text{mol H}_2\cdot\text{g}^{-1}\cdot\text{h}^{-1}$  between 48 h and 66 h of irradiation for MOF-808-SH, Au/MOF-808-SH, MOF-808-SH(Ti) and Au/MOF-808-SH(Ti). An enhancement of the hydrogen production rates is observed after the activation period for the Ti doped MOF-808-SH(Ti) and Au/MOF-808-SH(Ti) materials probably due to the presence of titanium in the SBU nodes.<sup>28</sup> A synergy is apparent between the titanium and gold nanoparticles since the enhancement is higher for Au/MOF-808-SH(Ti) with an increased rate by a factor 12.5 after the activation period. In comparison, Au/MOF-808-SH produces less hydrogen than the reference MOF-808-SH (Figure 6e).

Some hybrid Au/MOF materials are reported for the photocatalytic oxidation of alcohol,<sup>10, 33</sup> oxidation of benzyl alcohol,<sup>12, 34</sup> or CO<sub>2</sub> reduction.<sup>35</sup> But, only a few examples (reported in Table S12) were studied for photocatalytic Hydrogen Evolution Reaction (HER).<sup>36-39</sup> Although MOF-noble metal nanoparticles (Pt, Pd) present better photocatalytic efficiencies for HER,<sup>28, 39-43</sup> the conceptual utilization of HER to monitor the Au NPs stability could constitute a keystone for further research in the field. Indeed, surprisingly, two H<sub>2</sub> evolution

rates are measured for Au/MOF-808-SH (Ti) material resulting to the growth of Au NPs from ~1nm to ~2 nm. Finally, after the activation period, the H<sub>2</sub> evolution rate evolves up to 1.50  $\mu\text{mol.h}^{-1}.\text{g}^{-1}$  which is in the same range of photocatalytic efficiency in HER than the pure hybrid Au/MOF materials already reported (Table S12) considering the size and purity of Au NPs and basic photocatalytic conditions used to monitor the gold stability. For completeness, Table S12 lists of more complex hybrid Au/MOF materials where the addition of a new element: CdS quantum dots (Au@CdS/MIL-101 (Cr)),<sup>38</sup> TiO<sub>2</sub> anatase shell (MIL-101 core – Au/anatase shell)<sup>37</sup> or presence of CO<sub>2</sub> (Au/MIL-125 (Ti)),<sup>36</sup> drastically increases the photocatalytic efficiency of the original and pure Au/MOF photocatalyst (Table S12).

**Table S12.** Hybrid Au/MOF materials reported in the literature for HER.

Hybrid systems for HER	Au NPs size	Precursor / Stabilizing / reduction conditions	Photocatalytic conditions	Irradiation source	H <sub>2</sub> production rate ( $\mu\text{mol}\cdot\text{h}^{-1}\cdot\text{g}^{-1}$ )	Ref.
Au/MOF-808-SH (Ti)	before 48 h: ~1nm after 48 h: ~2nm	HAuCl <sub>4</sub> / none / UV irradiation	H <sub>2</sub> O / TEOA ([TEOA] = 10 <sup>-2</sup> mol/L)	Xe Lamp (300 W), 340-800 nm	1.5	
Au/MIL-125 (Ti)	52 x 14 nm (nanorods)	HAuCl <sub>4</sub> / CTAB + aromatic additives / NaBH <sub>4</sub>	MeCN / TEOA / H <sub>2</sub> O (9:1:0.15, v:v)	Xe lamp (300 W), 380-800 nm	10.2	39
Au/MIL-125 (Ti)	2.5 nm	HAuCl <sub>4</sub> / none / thermolysis 160°C	CO <sub>2</sub> saturated MeCN / TEOA (5:1, v:v) mixture	Xe Lamp (300 W), 420-800 nm (cutoff filter)	100	36
Au@MIL-101	-	Au(CO)Cl / none / hydrogenolysis (H <sub>2</sub> )	H <sub>2</sub> O / MeOH (2:1, v:v)	W Lamp (400 W), >400 nm (cutoff filter)	0	37
MIL-101 core - Au/anatase shell	-	Au(CO)Cl / none / hydrogenolysis (H <sub>2</sub> )	H <sub>2</sub> O / MeOH (2:1, v:v)	W Lamp (400 W), >400 nm (cutoff filter)	1000	37
Au/MIL-101 (Cr)	~25 nm	HAuCl <sub>4</sub> / none / annealing 100 °C	H <sub>2</sub> O / Na <sub>2</sub> S and Na <sub>2</sub> SO <sub>3</sub> (20 mmol in 100 mL water)	Xe Lamp (300 W), >420 nm (cutoff filter)	0	38
Au@Cds/MIL-101 (Cr)	-	HAuCl <sub>4</sub> / none / annealing 100 °C	H <sub>2</sub> O / Na <sub>2</sub> S and Na <sub>2</sub> SO <sub>3</sub> (20 mmol in 100 mL water)	Xe Lamp (300 W), >420 nm (cutoff filter)	25000	38

**C-12. Additional Characterization of Au/MOF-808-SH after photocatalysis**

During the Au NPs growth under UV-visible irradiation (Figure S34a), a 25.1% at. loss of titanium is observed by EDS in Au/MOF-808-SH(Ti) (Figure S37b). Moreover, the vibrational mode assigned to COO-Ti at 1656 cm<sup>-1</sup> decreases in intensity in the IR spectrum of Au/MOF-808-SH(Ti) (Figure S34b) which is consistent with a loss of titanium observed in EDS. During the photocatalytic experiment, an additional titanium loss is observed by EDS (Figure S38a, b, Table 11): 14.8 % at. and 37.2 % at. of titanium are lost respectively during the growth of Au NPs in MOF-808-SH(Ti) and Au/MOF-808-SH(Ti) during the photocatalytic experiment. This loss already observed by Cohen *et al.* is due to UV-visible irradiation used during the growth of Au NPs and to date, no explanation of this phenomenon has been reported.<sup>6</sup> After photocatalysis, two vibrational modes are observed in the

differential spectrum (Figure S40) at 1630/1571  $\text{cm}^{-1}$  and 1452/1389  $\text{cm}^{-1}$  and correspond to the vibrational COO-Zr modes; no vibrational mode of the OH groups is observed (Figure S40). In the Raman spectra, the vibrational mode of Au-O bonds is observed at 263  $\text{cm}^{-1}$  and 262  $\text{cm}^{-1}$  respectively for Au/MOF-808-SH(Ti) before and after photocatalysis and the intensities of all the vibrational modes are reduced after the photocatalysis (Figure S41). All these observations suggest a decrease in interaction between the Au NPs and the carboxylate groups, while Au-O bonds between the Au atoms and the bridge -O of the SBU nodes are clearly detected. Furthermore, the signal at 1016  $\text{cm}^{-1}$ , assigned to the C-H ring breathing and C-O stretching vibrational modes in the pmba functional groups, is drastically reduced,<sup>26, 44</sup> and the EDS spectra show a ~25% loss of sulfur (Table S10). During the irradiation, a part of the pmba functional groups are probably detached and removed into the solution, which frees up more space in the pores and is favorable to NP aggregation, leading to an increase of the Au NP size. All these elements, in addition to the conservation of the Au loading: 0.14% before and 0.15% after the photocatalysis (Table S10), strongly support the confinement of larger Au NPs (~2 nm) inside the MOF host.

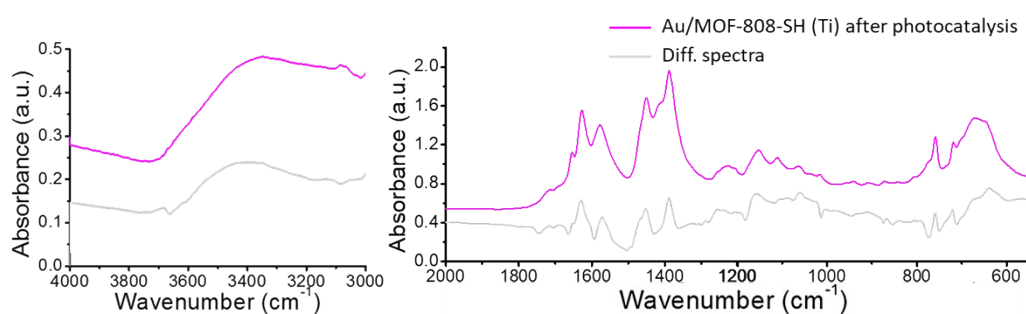


**Figure S40.** IR spectra of Au/MOF-808-SH(Ti) after photocatalysis (violet). The differential spectrum between Au/MOF-808-SH(Ti) after and before photocatalysis is depicted in grey.

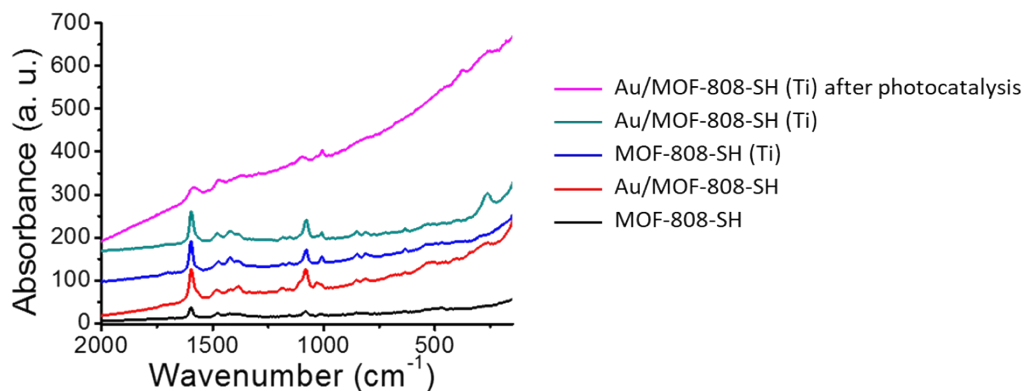


**Figure S41.** Raman spectra of MOF-808-SH (black), Au/MOF-808-SH (red), MOF-808-SH(Ti) (blue), Au/MOF-808-SH(Ti) (blue-green), Au/MOF-808-SH after photocatalysis (violet).

### C-13. XPS depth profile of Au/MOF-808-SH (Ti) before and after photocatalysis

XPS and Sputtering experiment: The MOFs were introduced into the Versa Probe II UHV chamber (base pressure  $4 \times 10^{-8}$  Pa). The MOFs were then sputtered two times 4 minutes with clusters of Ar (2500 Ar atoms) at an energy of 20 keV (8 eV per Ar atom). XPS spectra were recorded before any sputtering (red curves), after the first 4 minutes of sputtering (black curves), and after the second 4 minutes of sputtering (green curves).

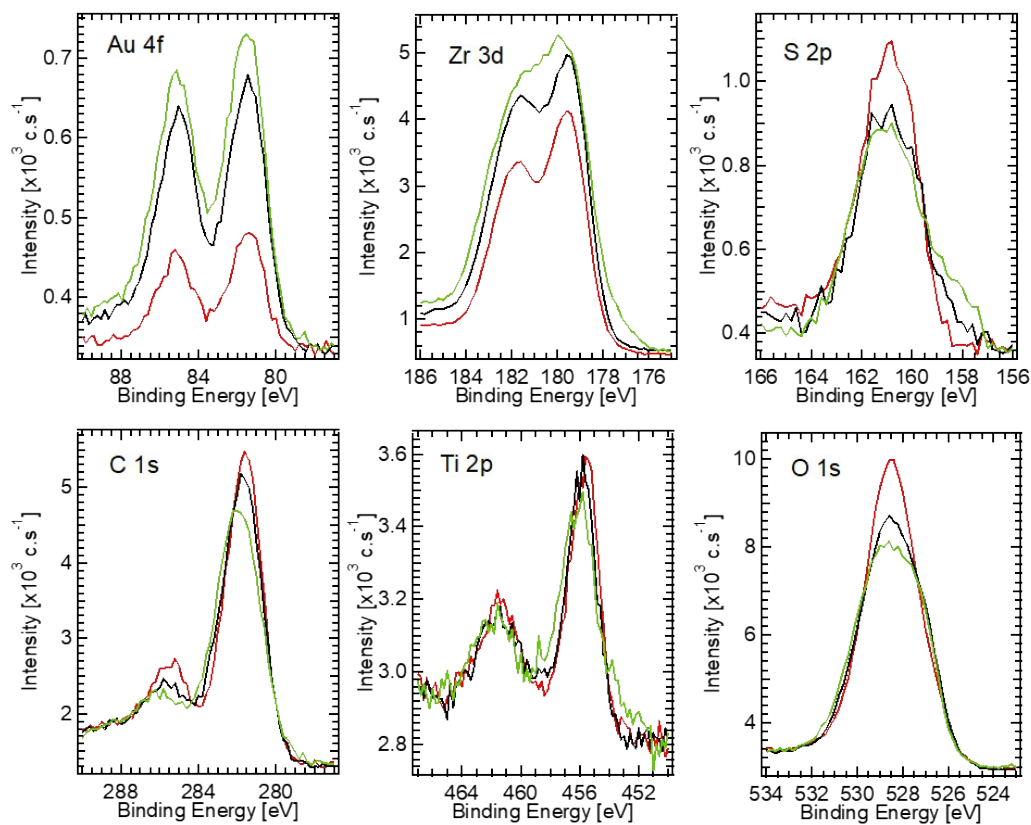


**Figure S42.** XPS spectra of Au 4f, Zr 3d, S 2p, C 1s, Ti 2p, and O 1s during subsequent sputtering of Au/MOF-808-SH (Ti) before photocatalysis.

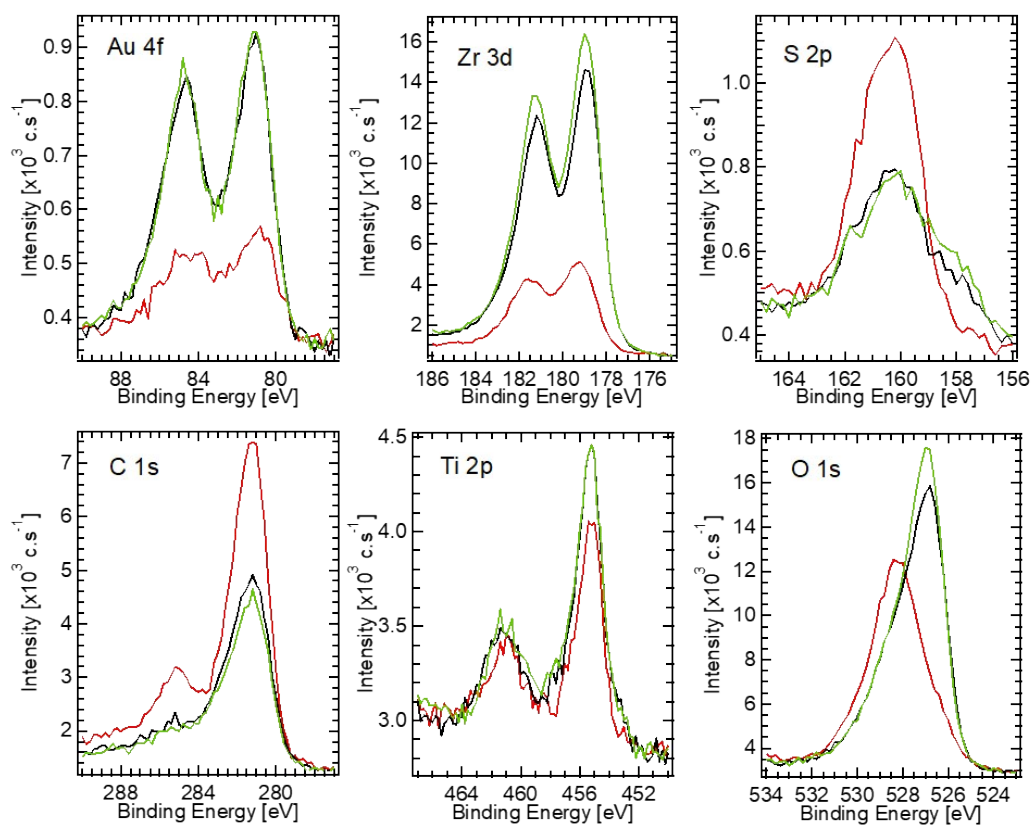


**Figure S43.** XPS spectra of Au 4f, Zr 3d, S 2p, C 1s, Ti 2p, and O 1s during subsequent sputtering of Au/MOF-808-SH (Ti) after photocatalysis.

## REFERENCES

1. J. Jiang, F. Gandara, Y. B. Zhang, K. Na, O. M. Yaghi and W. G. Klemperer, *J. Am. Chem. Soc.*, 2014, **136**, 12844-12847.
2. T. Zhao, F. Jeremias, I. Boldog, B. Nguyen, S. K. Henninger and C. Janiak, *Dalton Trans.*, 2015, **44**, 16791-16801.
3. T. Liu, J.-X. Che, Y.-Z. Hu, X.-W. Dong, X.-Y. Liu and C.-M. Che, *Chem. Eur. J.*, 2014, **20**, 14090-14095.
4. S. Bernt, V. Guillerme, C. Serre and N. Stock, *Chem. Commun.*, 2011, **47**, 2838-2840.
5. M. J. Katz, Z. J. Brown, Y. J. Colon, P. W. Siu, K. A. Scheidt, R. Q. Snurr, J. T. Hupp and O. K. Farha, *Chem. Commun.*, 2013, **49**, 9449-9451.
6. Y. Lee, S. Kim, J. K. Kang and S. M. Cohen, *Chem. Commun.*, 2015, **51**, 5735-5738.
7. F.-X. Coudert and A. H. Fuchs, *Coord. Chem. Rev.*, 2015, **307**, 211-236.
8. N. V. Maksimchuk, O. V. Zalomaeva, I. Y. Skobelev, K. A. Kovalenko, V. P. Fedin and O. A. Kholdeeva, *Proc. R. Soc. A*, 2012, **468**, 2017-2034.
9. J. H. Cavka, S. Jacobsen, U. Olsbye, N. Guillou, C. Lamberti, S. Bordiga and K. P. Lillerud, *J. Am. Chem. Soc.*, 2008, **130**, 13850-13851.
10. A. Dhakshinamoorthy, A. M. Asiri and H. Garcia, *ACS Catal.*, 2017, **7**, 2896-2919.
11. N. E. Christensen and V. Heine, *Phys. Rev. B*, 1985, **32**, 6145-6156.
12. D. Esken, S. Turner, O. I. Lebedev, G. Van Tendeloo and R. A. Fischer, *Chem. Mater.*, 2010, **22**, 6393-6401.
13. J.-W. Park and J. S. Shumaker-Parry, *J. Am. Chem. Soc.*, 2014, **136**, 1907-1921.
14. R. Yan, Y. Zhao, H. Yang, X.-J. Kang, C. Wang, L.-L. Wen and Z.-D. Lu, *Adv. Funct. Mater.*, 2018, **28**, n/a.
15. S. Chen and K. Kimura, *Langmuir*, 1999, **15**, 1075-1082.
16. H. H. Brongersma, M. Draxler, M. de Ridder and P. Bauer, *Surf. Sci. Rep.*, 2007, **62**, 63-109.
17. A. Rafati, R. Ter Veen and D. G. Castner, *Surf. Interface Anal.*, 2013, **45**, 1737-1741.
18. H. H. Brongersma and P. M. Mul, *Chem. Phys. Lett.*, 1973, **19**, 217-220.
19. P. Bruener, T. Grehl, H. Brongersma, B. Detlefs, E. Nolot, H. Grampeix, E. Steinbauer and P. Bauer, *J. Vac. Sci. Technol. A*, 2015, **33**, 01A122.
20. G. Kresse and J. Furthmüller, *Phys. Rev. B*, 1996, **54**, 11169-11186.
21. G. Kresse and D. Joubert, *Phys. Rev. B*, 1999, **59**, 1758-1775.
22. T. Thonhauser, V. R. Cooper, S. Li, A. Puzder, P. Hyldgaard and D. C. Langreth, *Phys. Rev. B*, 2007, **76**, 125112.
23. T. Thonhauser, S. Zuluaga, C. A. Arter, K. Berland, E. Schroder and P. Hyldgaard, *Phys. Rev. B*, 2015, **115**, 136402.
24. K. Berland, V. R. Cooper, K. Lee, E. Schroeder, T. Thonhauser, P. Hyldgaard and B. I. Lundqvist, *Rep. Prog. Phys.*, 2015, **78**, 066501.
25. D. C. Langreth, B. I. Lundqvist, S. D. Chakarova-Kack, V. R. Cooper, M. Dion, P. Hyldgaard, A. Kelkkanen, J. Kleis, L. Kong, S. Li, P. G. Moses, E. Murray, A. Puzder, H. Rydberg, E. Schröder and T. Thonhauser, *J. Phys. Condens. Matter*, 2009, **21**, 084203.
26. G. Wang, C. Sharp, A. M. Plonka, Q. Wang, A. I. Frenkel, W. Guo, C. Hill, C. Smith, J. Kollar, D. Troya and J. R. Morris, *J. Phys. Chem. C*, 2017, **121**, 11261-11272.
27. M. Dan-Hardi, C. Serre, T. Frot, L. Rozes, G. Maurin, C. Sanchez and G. Férey, *J. Am. Chem. Soc.*, 2009, **131**, 10857-10859.
28. Y. Horiuchi, T. Toyao, M. Saito, K. Mochizuki, M. Iwata, H. Higashimura, M. Anpo and M. Matsuoka, *J. Phys. Chem. C*, 2012, **116**, 20848-20853.
29. M. S. Denny Jr., L. R. Parent, J. P. Patterson, S. K. Meena, H. Pham, P. Abellan, Q. M. Ramasse, F. Paesani, N. C. Gianneschi and S. M. Cohen, *J. Am. Chem. Soc.*, 2017.

30. C. Maurer, B. Baumgartner, S. Pabisch, J. Akbarzadeh, H. Peterlik and U. Schubert, *Dalton Trans.*, 2014, **43**, 950-957.
31. A. Brethon, L. G. Hubert-Pfalzgraf and J.-C. Daran, *Dalton Trans.*, 2006, **1**, 250-257.
32. A. D. Weisz, A. E. Regazzoni and M. A. Blesa, *Solid State Ion.*, 2001, **143**, 125-130.
33. Z. Gu, L. Chen, B. Duan, Q. Luo, J. Liu and C. Duan, *Chem. Commun.*, 2016, **52**, 116-119.
34. L. Chen, Y. Peng, H. Wang, Z. Gu and C. Duan, *Chem. Commun.*, 2014, **50**, 8651-8654.
35. K. Khaletskaya, A. Pougin, R. Medishetty, C. Rosler, C. Wiktor, J. Strunk and R. A. Fischer, *Chem. Mater.*, 2015, **27**, 7248-7257.
36. D. Sun, W. Liu, Y. Fu, Z. Fang, F. Sun, X. Fu, Y. Zhang and Z. Li, *Chem. Eur. J.*, 2014, **20**, 4780-4788.
37. D. Tilgner and R. Kempe, *Chem. Eur. J.*, 2017, **23**, 3184-3190.
38. Y. Wang, Y. Zhang, Z. Jiang, G. Jiang, Z. Zhao, Q. Wu, Y. Liu, Q. Xu, A. Duan and C. Xu, *Appl. Catal.*, 2016, **185**, 307-314.
39. J.-D. Xiao, L. Han, J. Luo, S.-H. Yu and H.-L. Jiang, *Angew. Chem. Int. Ed.*, 2018, **57**, 1103-1107.
40. R. Liang, S. Luo, F. Jing, L. Shen, N. Qin and L. Wu, *Appl. Catal.*, 2015, **176-177**, 240-248.
41. M. Wen, K. Mori, Y. Kuwahara and H. Yamashita, *ACS Energ. Lett.*, 2016, **2**, 1-7.
42. D. Sun and Z. Li, *J. Phys. Chem. C*, 2016, **120**, 19744-19750.
43. D. Wang, Y. Song, J. Cai, L. Wu and Z. Li, *New J. Chem.*, 2016, **40**, 9170-9175.
44. J. Gao, Y. Hu, S. Li, Y. Zhang and X. Chen, *Spectroc. Acta A*, 2013, **104**, 41-47.